DETERMINE THE AERODYNAMIC CHARACTERISTICS OF THE MQSPEED HPV AERO-FAIRING

Geoffrey Kitchen

Bachelor of Engineering,
Mechatronic Engineering

Department of Engineering
Macquarie University

November 6, 2016

Supervisor: Dr Sammy Diasinos

MACQUARIE UNIVERSITY

DEPARTMENT APPROVAL

of a senior thesis submitted by

Geoffrey Kitchen

This thesis has been reviewed by the research advisor, research coordinator, and department chair and has been found to be satisfactory.

_____   _____

Date   Supervisor: Dr Sammy Diasinos, Advisor

_____   _____

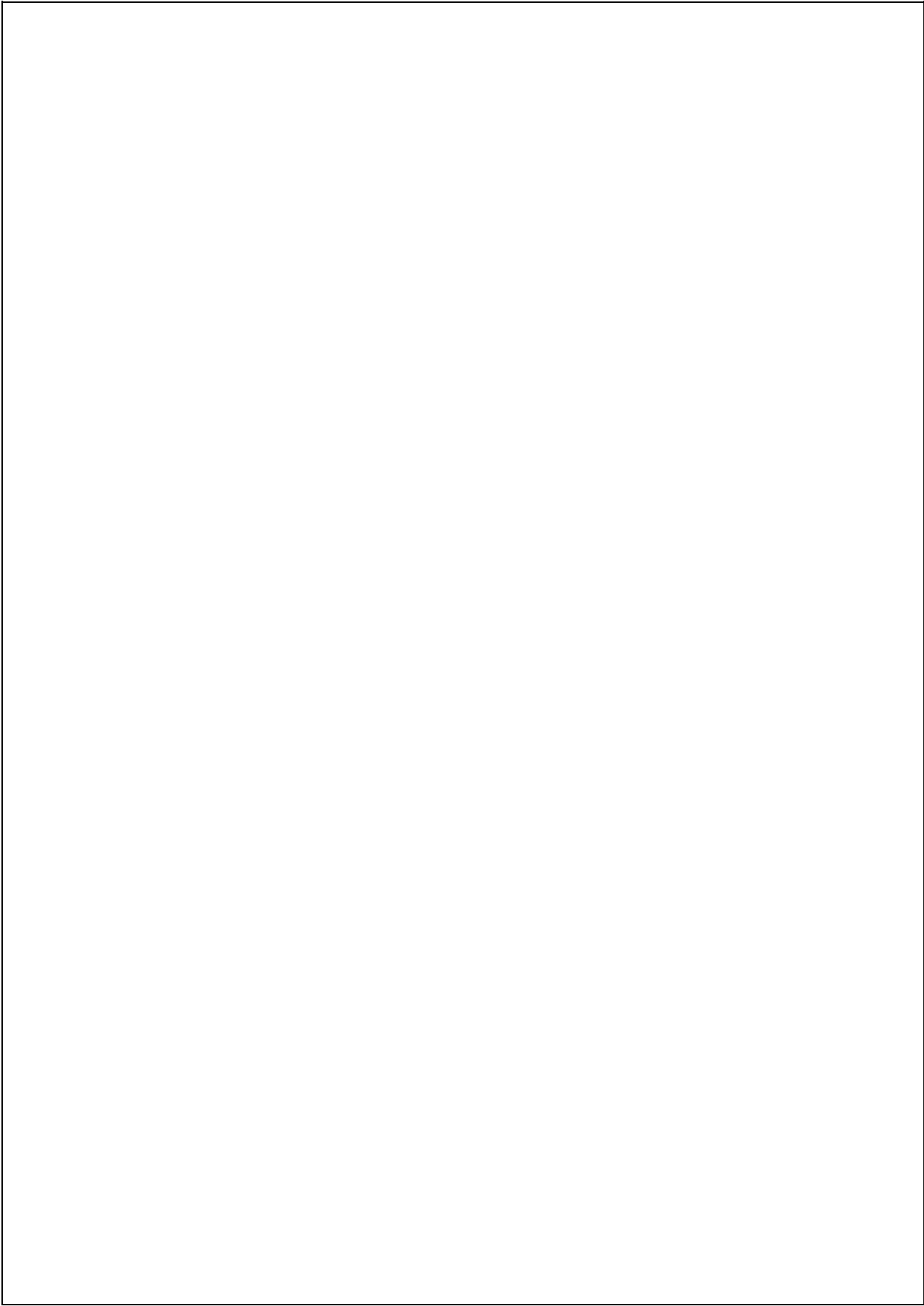Date   Department Ugrad Coordinator , Research Coordinator

_____   _____

Date   Department Chair Name, Chair

ACKNOWLEDGMENTS

ABSTRACT

In 2013 a group of students began work on designing & building a Human Powered Vehicle to challenge for the world speed record, with competition being conducted annually in Battle Mountain, Nevada, USA. At this stage the preliminary designs for the aerodynamic fairing have been developed with the aid of Computational Fluid Dynamic (CFD) modeling and the base frame & shell plug have been constructed.

Due to the theoretical nature of the CFD modeling there is a need to validate the data to ensure the correct characteristics are being used. This thesis project was established to provide that validation by constructing a reconfigurable model for testing in the Macquarie University wind tunnel. Testing will be conducted utilizing Force & Torque measurements and also by logging air pressure measurements at key positions along the fairing's length. Particle Image Velocimetry readings will also be undertaken, given the availability of time and equipment.

After the project is completed, the CFD data will be validated and the continuing theoretical modeling can continue with confidence in the data being produced.

Contents

List of Figures

List of Tables

Chapter 1

Introduction

Competition for the outright world speed record for a Human Powered Vehicle (HPV) has been conducted at Battle Mountain Nevada, USA since October 2000. The competition was setup by the International Human Powered Vehicle Association (IHPVA) and named the World Human Powered Speed Challenge (WHPSC), but to most competitors it is simply known as Battle Mountain (BM).

Figure 1.1: Record breaking teams and the year broken [11].

The competition is run on a 6 Mile section of Highway 305 South of the town and it's distinguishing feature is a 170 foot drop from start to finish which is the maximum

1

allowable by World Record rules. Another rule that is applicable to the project in a maximun wind speed on the course of 6 km/h. This will be further discussed during testing as it influences some design considerations.

Although the competition started out largely as an amateur endeavour, it has attracted the attention of the engineering departments of many large universities around the world who see the competition as a chance to show their research abilities. These universities include Delft University of Technology, Netherlands (DELFT), University of Liverpool (UofL) and University of Toronto (UofT).

With the competition moving from a corinthian to more of a professional program, the development of the HPV's have become more technically focused. during the corinthian phase the record dropped by approximately 1 km/h every two years. The use of more sophisticated design processes by the university teams has seen the record fall by approximately 4 km/h each year. Recent record speeds and the teams setting the record can be found in Table H.1.

The current world record holders, Team Eta (a collaboration with UofT) set the record of 144.17 km/h in September 2016 and this record represents an increase of 3.3% over their previous record. As a comparison, Fig. 1.2 shows that a decrease of 6% in the Coefficient of Drag (C_D) will give the same gains achieved in breaking the previous record.
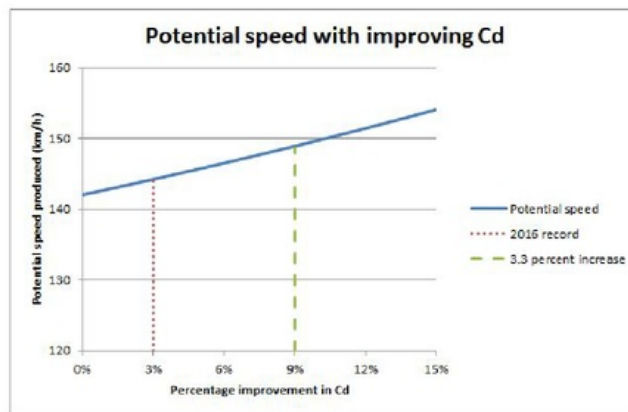
Figure 1.2: The potential speed increases available with increased efficiency

The used of Computational Fluid Dynamics (CFD) to develop these efficiencies has become a necessity given the increased development in HPV by universities and professional teams around the world. Aligned with this dependance on CFD is the need to validate the results being given. If incorrect factors are used as CFD inputs then the data being generated will be false. By combining the CFD study with a wind tunnel program the data can then be validated. The wind tunnel experiments can also be used to explore the design envelope and expose any undesirable traits that might be present with the design while identifying promising lines of development.

1.1 Background

1.1.1 CFD modeling

With competition for the world speed record becoming more professional, whereas previously competitors could hand shape fairings that looked about right, designs are now converging in shape through the used of technology such as CFD and Finite Element Analysis (FEA). As shown in Fig. 1.2, refining fairings with more efficient shapes can provide large gains in potential speed. As the shapes become more refined, CFD plays a greater role on finding the smallest improvements available.

1.1.2 The link between CFD and wind tunnel testing

When a CFD study is undertaken, assumptions are made about the environment the HPV operates in. If these assumptions are not validated then the information the CFD study produces can be false. By combining CFD testing with a structured wind tunnel program, the data being produced by CFD can be checked for accuracy and the wind tunnel information can be a primer for different area to concentrate the CFD study. This validation becomes more important as the testing tolerances get smaller and development is more dependent on the CFD results.

1.1.3 Macquarie University wind tunnel facility

The Macquarie University wind tunnel laboratory is located in F9c room 111 (henceforth called F9c). It consists of an electronically controlled, 11.9 kW motor that draws air through the wooden inlet seen in Fig. 1.3, through meshing and a constriction, past the test model and exhausts out past the motor (Fig. 1.4).

The intake is a 1.22 m diameter, octagonally shaped and houses the two part mesh. The first part of the mesh consists of a hexagonal honeycomb matrix and it is this honeycombing that straightens the airflow. The second stage is a fine mesh used to smooth the airflow entering the tunnel. The combination of the two give the airflow a smooth and uniform flow allowing consistent results.

1.82 m downstream of the mesh, the tunnel constricts from 1.22 m to 0.6 m over a length of 0.91 m. This constriction accelerates the uniform airflow into the test section. After the test section, the tunnel expands again to reduce the wind velocity and then the airflow exits the tunnel. Inside the measurement chamber is a variety of monitoring devices used in the control of the airflow including pitot tubes to determine the wind speed and sensors to measure temperature, humidity and air pressure.

The wind tunnel model is mounted on a support structure called a Sting and this sting both locates the model in the measurement envelope and provides a means for the wiring of the internal sensors to exit the tunnel without disturbing the airflow across the model.
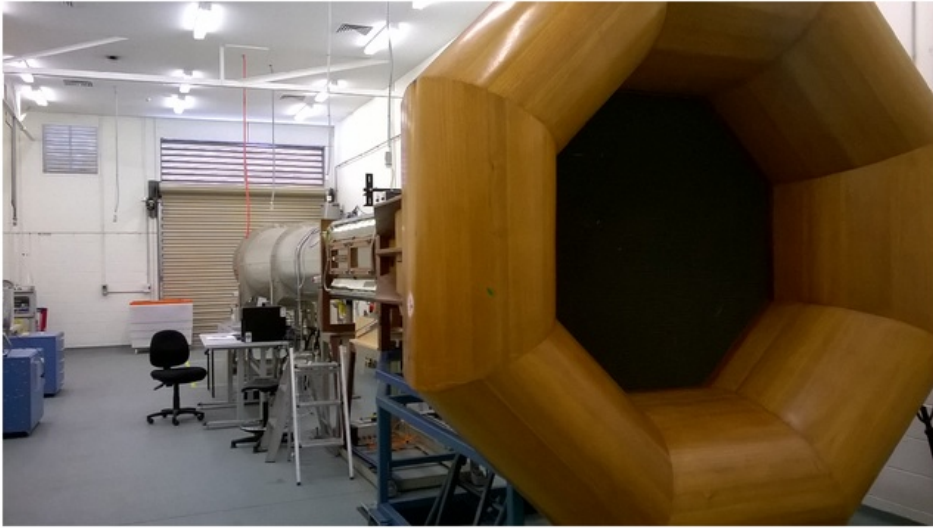
Figure 1.3: The Maqcuarie wind tunnel from the inlet

Figure 1.4: The Maqcuarie wind tunnel from outlet/ motor end.

1.2 Project Scope

1.2.1 Project Aims and Objectives

1. *Design and construct a reconfigurable wind tunnel model.*
   The first deliverable for the project is a center model section with a mounting spine for the attachment of a variety of nose and tail sections to enable the testing to different shape characteristics. These end sections have been identified as areas where the model has a sensitivity to differences and this sensitivity is to be investigated during the project. The model must also be able to be rotated off axis to facilitate measuring data for non-zero angles of attack.

2. *Ensure the design of the wind tunnel model is suitable for continuing experiments outside the current project's specifications.*
   This model is envisaged to be used in further experimentation after the project so it is important that future experimental procedures are considered and provisions for these are made.

3. *Select, validate & calibrate the sensors and transducers used in the conduct of these experiments.*
   Some of the equipment used in this project has come from other projects while others will need to be obtained. The item from other projects will have to be reconfigured to suit the new activities and specifications for the new equipment will be established.

4. *Obtain data for use in validating CFD studies of the MqSpeed Aerodynamic fairing using Force, Torque and Air Pressure measurements.*
   Develop a test program to encompass the areas to be investigated and ensure the time line is followed so that all experiments are completed in a timely manner.

5. *Conduct Particle Image Velocimetry experiments.*
   If there is time after all the testing is completed and the appropriate training and certification can be obtained, conduct experiments into the airflow over the model and downstream using Particle Image Velocimetry (PIV).

1.2.2   Baseline review & Time-line

Rank		Task	Start Date	Allocated Days	End Date
1		Sensors & Transducers			
	1.1	Selection	15/06/16	15	30/06/16
	1.2	Procurement	25/06/16	35	30/07/16
	1.3	Calibration	20/07/16	14	3/08/16
2		Model design & build			
	2.1	Shell Design	26/06/16	7	3/07/16
	2.2	Construction	3/07/16	31	3/08/16
3		Wind tunnel testing & data			
	3.1	Test session 1	3/08/16	10	13/08/16
	3.2	Test session 2	13/08/16	10	23/08/16
	3.3	Test session 3	23/08/16	10	2/09/16
	3.4	Test session 4	2/09/16	10	12/09/16
4		Thesis writing			
	4.1	Consolidate data	12/09/16	7	19/09/16
	4.3	Supply data for CFD	19/09/16	2	21/09/16
	4.2	Write up thesis	23/08/16	75	6/11/16
5		Assesment Tasks 2nd semester			
	5.1	Progress report	28/08/16	7	4/09/16
	5.2	Finalize report	19/10/16	18	6/11/16
	5.3	Seminar abstract	8/11/16	5	13/11/16
	5.4	Seminar presentation	14/11/16	10	24/11/16
	5.5	Demonstration & poster	22/11/16	2	24/11/16

Figure 1.5: Pojected timeline for thesis
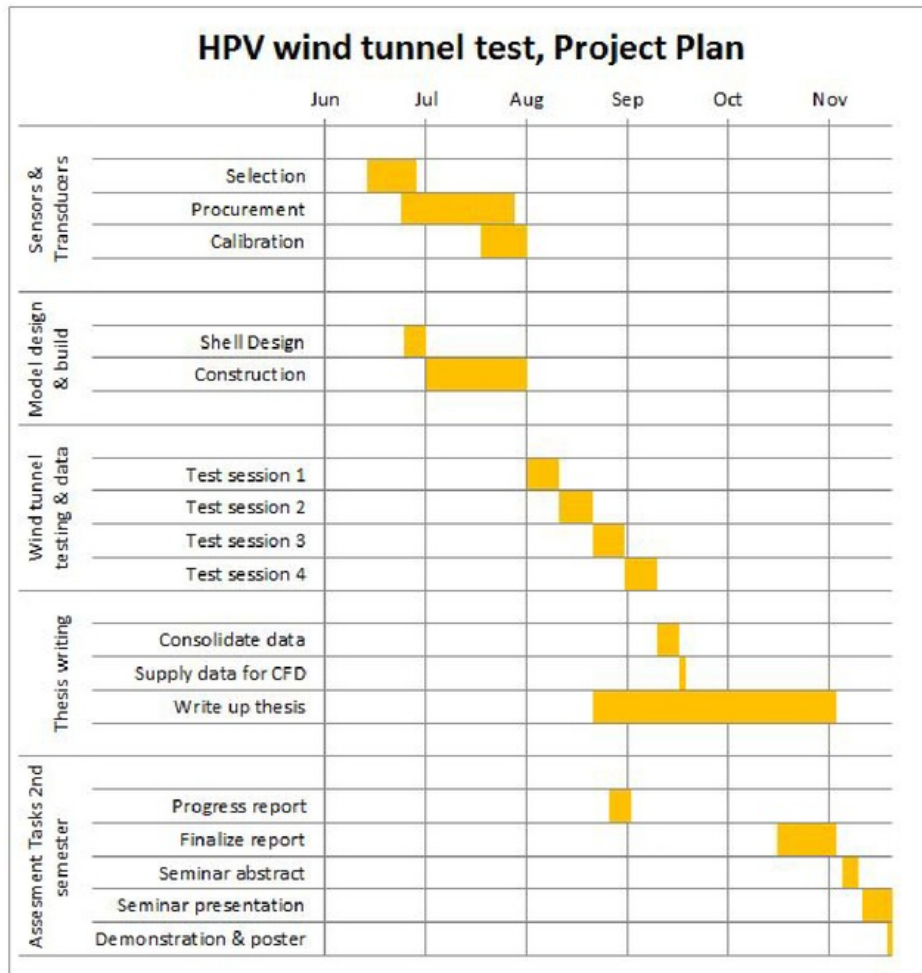
Figure 1.6: Gantt chart time-line for thesis

Chapter 2

Literature review and Related work

2.1 Wind tunnel methodologies

In the 2012 study "*Bicycle aerodynamics: an experimental evaluation methodology*" [4], Chowdhury and Alam conduct experiments on the various positions road cyclist assume in the wind tunnel facility at RMIT, Melbourne. The RMIT wind tunnel is a full scale facility, 3m wide by 2m high and 9m long. The tunnel is fitted with a 6 axis force/ torque transducer mounted on a platform in the middle of the test section.
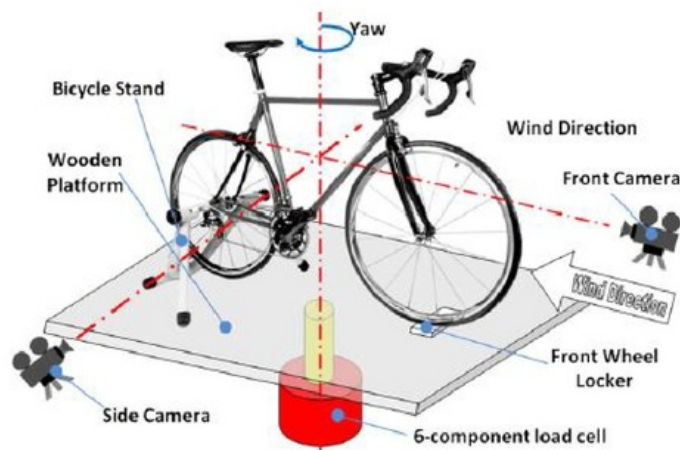
Figure 2.1: Forces and moments measured on the test subject [4]

The transducer measures the forces acting on the subject from wind speeds up to 70 km/h. The testing also identified the subject of tunnel blockage as a factor in incorrect data being obtained. A ratio of 10% frontal area to tunnel area was set a maximum level of blockage. The yaw angle was set at 0 degrees as an increase in yaw resulted in the blockage ratio being exceeded. Data was sampled at 20 Hz for 30 seconds to minimize

electrical interference.

Defraeye et al. in the 2010 study, "*Aerodynamic study of different cyclist positions: CFD analysis and full-scale wind-tunnel tests*" [6], conducted experiments in a similar sized wind tunnel as the Chowdhury study, but setting the maximum level of blockage as 6%. In addition to the force & torque measurements taken, the Defraeye study used a 3D laser scanning system to capture the specific body characteristics and positioning of the rider. This positioning was then used to construct a model to be used in a CFD analysis to validate the wind tunnel measurements taken.
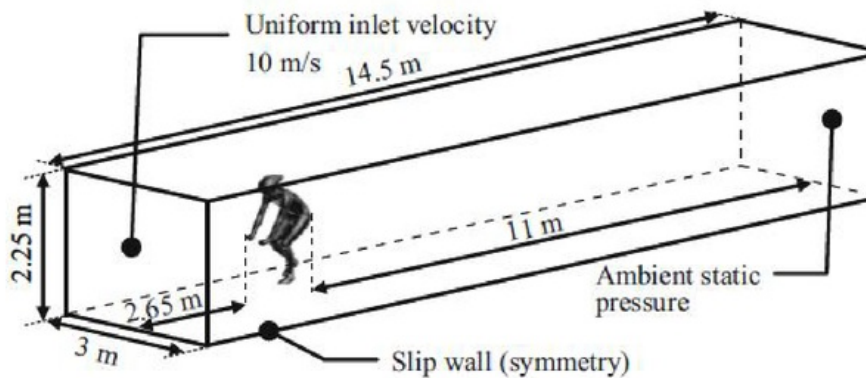
Figure 2.2: Wind tunnel subject placement for CFD study

As seen in Fig.2.2, the placement of the rider in the wind tunnel allows to a study of the wake downwind of the subject and is directly relatable to a CFD study. The methodology is further confirmed by Chowdhury and Alam in the 2013 study, "*An experimental study of airflow behaviour around a standard 2-man bobsleigh*" [5], where the same 6 axis F/T transducer set up in the RMIT wind tunnel. The study introduced the variable of scale by testing a less than full size model, and used dimensional similitude to allow for the change in scale, Fig.2.3. Due to the blockage factor being exceeded, a test model of 50% scale was constructed. Wool tufts and smoke wands were utilized to visualize the airflow over the model and the force and torque measurements were compiled.

The data was again sampled at 20 Hz for 30 seconds and multiple runs were recorded and averaged to minimize electrical interference on the transducer. Measurements were taken to an accuracy of plus minus 0.01 N and plus minus 0.5 km/h. To help visualize the wind flow, 40mm wool tufts were attached to the 1.35m long model and were spaced at 40mm intervals along the model. The tufts were monitored with both video and still photographs, Fig.2.4.
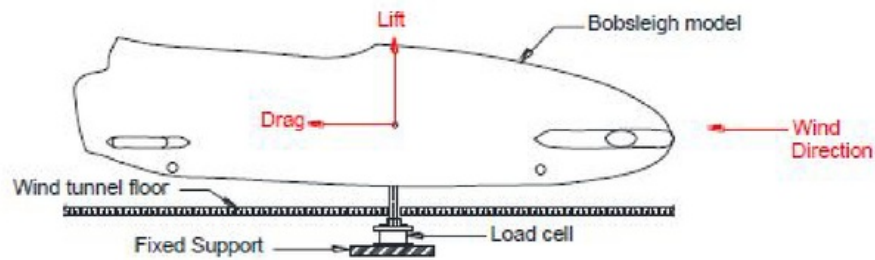
Figure 2.3: Bobsled installed on the FT transducer and utilizing a false tunnel floor.
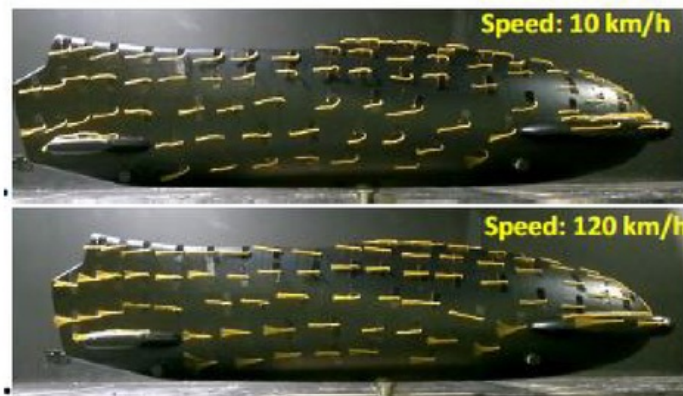
Figure 2.4: Flow visualization test with 40mm wool tufts on a 1.35m model

The smoke wand was only used at slow speeds (5 km/h) and was concentrated on specific areas of interest. The data obtained was compared with a CFD study of the same model and it was found that the wind tunnel model experienced a slightly higher drag Coefficient (C_D) than predicted by CFD. This difference was attributed to high air turbulence intensity in the RMIT wind tunnel of 1.8%. Experimental variation was also a factor.

2.2 HPV Studies

2.2.1 Available power for a HPV

Journal papers such as "*Aerodynamics of human-powered vehicles*" [13] and thesis project "*Aerodynamic test platform for Human Powered Vehicle (HPV)*" [19] provide supportive information but as they are concerned with current record attempts, the actual performance figures are often not quoted. Kyle introduces the need for reducing the drag

coefficient to obtain higher speeds, quoting the drag of a modern time trial bike at 50 km/h as 28 N. The increase in efficiency of HPV's over time is shown in Table 2.1.

Vehicle	Frontal area A_f (m^2)	Coefficient of Drag C_d	Drag Area C_dA	Mass (kg)	50 km/h Power (W)	130 km/h Power (W)
Road Bike '02	0.35	0.68	0.238	82	427 (100%)	5798 (100%)
HPV 1973	0.71	0.10	0.071	87	162 (38%)	1699 (29%)
HPV 1977	0.46	0.14	0.064	91	151 (35%)	1525 (26%)
HPV 1986	0.40	0.08	0.032	89	100 (23%)	741 (13%)
HPV 2002	0.32	0.05	0.016	92	76 (18%)	346 (6%)

Table 2.1: Required power of Bicycles and HPV's [13]

2.2.2 Early methods of drag reduction

Alam, Silva & Zimmers 2012 study *Aerodynamic study of human powered vehicles* [2] delves into improvements that can be made to a HPV shell but it is more in line with recreational three wheeled vehicles. The study is conducted in the RMIT wind tunnel facility and was originally conducted to design an entry in the Royal Automobile Club of Victorias energy breakthrough challenge. Seven vehicles were tested with 6 being bare trike frames and one being a fully faired trike.

Figure 2.5: A selection of representative vehicles from the study

The bare trikes also had body variations to improve their aerodynamics and efficiencies. These included additions such as windscreens, canopies, deflectors and wheel fairings. Testing was conducted on seating position, add-ons, faired vehicle variations and a comparison of the different types and the most applicable results are seen in Fig. 2.6.

Of most interest for the Mq-Speed HPV is the testing of the faired vehicle variations. Adding a canopy over the driver cockpit, a visor to the canopy and finally fitting wheel covers all incrementally improved the drag coefficient of the vehicle.
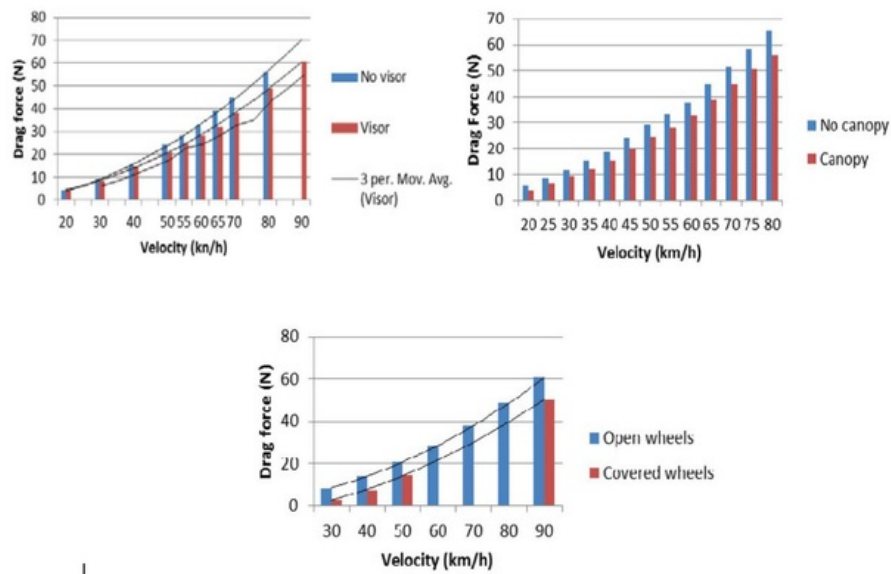
Figure 2.6: Data presented in *Aerodynamic study of HPV's* [2].

2.2.3 Fully enclosed HPV's

In the 2013 study *On-road and wind tunnel aerodynamic study of human powered vehicles* [3], the authors conducted a wind tunnel study on a pair of HPV's intended for city commuting. The dimensions for each HPV are stated in Fig. 2.7.

Specifications	Production HPV 1	Production HPV 2
Mass	29 kg	33 kg
Materials	Aluminium frame	Aluminium frame
	& Plastic panel	& fibreglass panel
Length	2400 mm	2320 mm
Width	700 mm	760 mm
Height	1000 mm	780 mm
Frontal Area (CFD)	0.663 m2	0.457 m2
Frontal Area (Model)	0.581 m2	0.492 m2

Figure 2.7: Physical dimensions for HPV1 and HPV2 [3].

The reference to Frontal Area (CFD) and Frontal Area(Model) is due to the CFD models being a simplified version of the wind tunnel models and not an exact size match.

These models were based on full size HPV's that were track tested to provide guidance on wind-speed and conditions to use in the CFD and wind tunnel studies. The author notes that the data for HPV-2 was slightly skewed due to its weight and the track having a slight uphill section. For this reason, direct comparison of the full scale models was not used.

The author's original supposition was that HPV-2 would have the least drag as it has a smaller frontal area. The data gives the opposite result though and upon further investigation it was discovered that additional rear fairing and less efficient foil shape of the shell combined to give HPV-2 a higher C_D in all wind ranges tested.
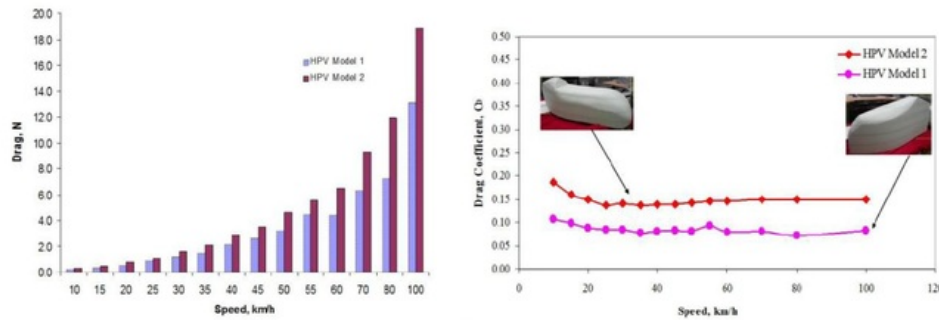
Figure 2.8: Data obtained from testing HPV1 and HPV2

Of interest to the current project is in Fig. 2.8b, where the C_D for both models changes with wind-speeds. This is common to early testing on the Mq-Speed HPV where the C_D was seen to also change with wind-speed.

2.2.4 Early Delft studies

The team of masters students from the university of Delft wrote the paper *Bicycle Design, A different approach to improving on the human powered vehicle world speed record* [9] detailing their attempt to break the world record in 2012, a feat they achieved in 2013.

In section 5 of the paper, the authors introduce the need for the least amount of surface area possible so as to increase possible performance. They raised the rider seat angle from 16° to 20° to better position the rider's shoulders in the maximum width point of the Selig s1016 NLF laminar flow profile. With this profile they were able to achieve an CFD calculated $C_D A$ of 0.0062. When tested in the wind-tunnel, a 1/3 scale model only achieved a $C_D A$ of 0.013. Full size development was conducted using flow paint in combination with scale model wind tunnel testing and it was found that the best $C_D A$ that could be obtained was 0.03. After calculations were performed with this $C_D A$ and the power output of the rider, it was decided that the world record was achievable and production of the bike commenced.

It is worth noting that the bike describe above is the bike before the model that eventually broke the world record. Further optimization of the shape was conducted

	Original CFD model with $C_DA = 0.0062$. Green indicates laminar flow. Pink turbulent flow.
	1:3 scale model in oil streak wind tunnel test. Yellow colour indicates where oil is present. Large yellow surface indicates laminar flow, streak lines indicates turbulence. $C_DA = 0.013$.
	Optimized CFD model after using scaled model experiment information. $C_DA = 0.015$.
	Full scale oil streak wind tunnel test, prior to surface smoothing. Red line indicates the laminar flow region. Note that the window causes turbulent flow. $C_DA = 0.030$.
	Final product. Smoothed outer shape (sticker), Wind tunnel test $C_DA = 0.030$, open road test $C_DA = 0.032$. The red line indicates the wind tunnel laminar flow region.

Figure 2.9: Development of the first Velox HPV shell [9].

but after the record was broken, studies were no longer published so as to protect their intellectual property.

2.3 Low drag vehicles

2.3.1 Applicable Solar Car studies

Roche et al, in Chapter 5 of the 1997 book *Speed of light, the 1996 World Solar Challenge* [18], discovered that the vehicle exposed to increasing AoA exhibited an overall drop in aerodynamic drag and theorized that side winds could make the vehicle more efficient. The sensitivity of the HPV fairing will be tested with increasing AoA to discover if the same drop is achieved with the HPV shell.

It is not expected that the HPV will share this characteristic as the aerodynamic side profile for the solar car is low profile while the HPV is proportionally taller and flat sided in comparison. The HPV is not expected to maintain aerodynamic flow over the shell for larger AoA.

The solar car is also expected to handle a variety of cross wind forces along the course whereas the rules of competition for the HPV world record limit the strength of wind that can be present during valid attempts.
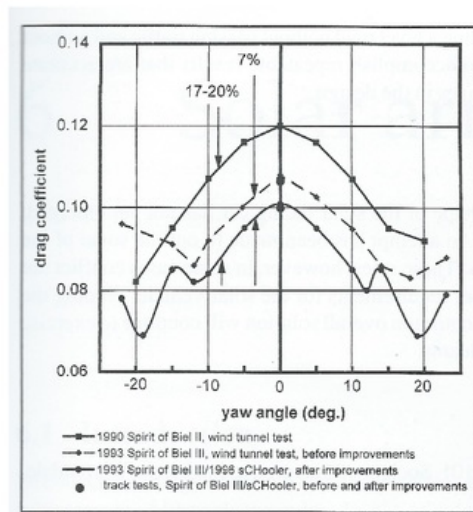
Figure 2.10: Findings from the UNSW solar car study into increasing AoA and its effects on drag [18].

2.4 Competitor review

A review of the current state of the art in competitors for the world speed record for a Human Powered Vehicle. Information for this section has been obtained from news items, emails, Facebook pages, blogs and team websites with the main source being the IHPVA website and Facebook page.

Figure 2.11: The current world record holders & their bike, Team Aerovelo from Toronto, Canada [1]

2.4.1 Aerovelo & University of Toronto, Canada

Aerovelo & the University of Toronto (UofT) are two separate teams but both use the same resources for their aero fairings. UofT provides design and technical development while Aerovela attracts funding for the project.

Aerovela is using the HPV as a promotional source for it's commuter bicycle business and for raising the profile of alternative transport. They are the current world record holder at 139.45 km/h and is returning to BM in 2016 with a refinement to their bike from last year, some of which can be seen in Fig. 2.12.

Edit: Since writing this section, Aerovela has raised the world record to 144.17 km/h during the 2016 competition.
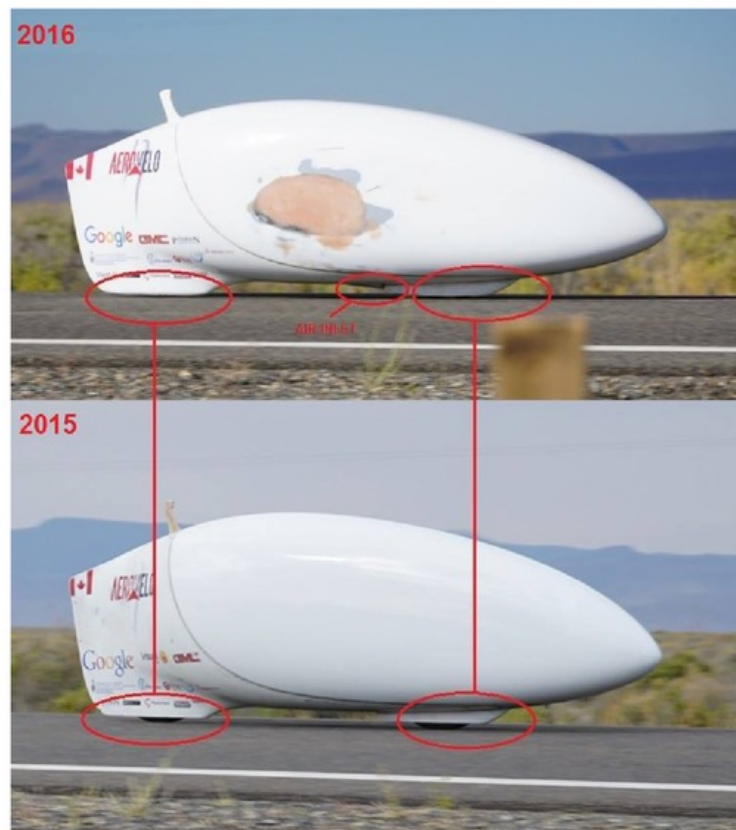
Figure 2.12: Upgrades to the Aerovela HPV between 2015 and 2016.

In Fig. 2.12 some subtle changes can be seen in the Aerovela HPV. The UofT team has identified that the interface area from the bottom of the shell to the ground needs careful attention to detail to reduce drag and they have achieved this by lowering the fairing and

giving it a more aerodynamic shape. MqSpeed had identified this feature early on and this lowering of the fairing is a feature of the test model.

Of note also is the attention to maintaining laminar flow over the HPV shell. This is demonstrated by the shell having no sponsors logos or artwork in the areas sensitive to tripping the laminar flow.

The scarring seen on the side of the 2016 shell was the result of a low speed crash during pre-competition testing caused by a airflow induced flutter between 50 & 60 km/h. The cause of this flutter has not been published yet.

2.4.2   DELFT University. Netherlands

DELFT is the previous record holder and are a strong team with good research facilities. Most of their research program is conducted by engineering Masters candidates and they have access to a full size wind tunnel for their experimentation. Because the HPV is being developed by master's students it is expected that papers will be published on the subject in the near future. The team has already published *Bicycle Design, A different approach to improving on the human powered vehicle world speed record* [9] after their first record breaking HPV attempt.

When Delft was first entering competition they identified two schools of thought on powering a HPV. The first is used by UofT and this is to deasign the smallest, most efficient HPV that will fit a rider and then find a rider to fit. The second method, developed by Team Delft is to fine the biggest, most powerful rider they can find and then design the smallest HPV that will fit the rider. The first method is all about efficiency while the second is all about maximum power. This maximum power design earned Delft the world record in 2013 but the smaller more efficient design took the record off them in 2015.

Figure 2.13: VeloX 6 training in Holland [7].

Comparing Fig. 2.13 with Fig. 2.12, both HPV's exhibit the laminar flow foil shape

with the Delft bike having a slightly higher nose and fuller nose curvature. Knowing the preference of the Dutch towards bigger riders, the fuller nose could be to accommodate the extra internal room needed for a more powerful rider.

VeloX is still showing the slight gap between the bottom of the wheel fairing and the ground that Aerovela has filled in.

2.4.3 University of Liverpool Velocipede Team, UK

The University of Liverpool (UofL) is a new entry into HPV record attempts and 2016 will be their first attempt at the official record although they will be competing with a second generation shell. They also have access to a full size wind-tunnel on campus.
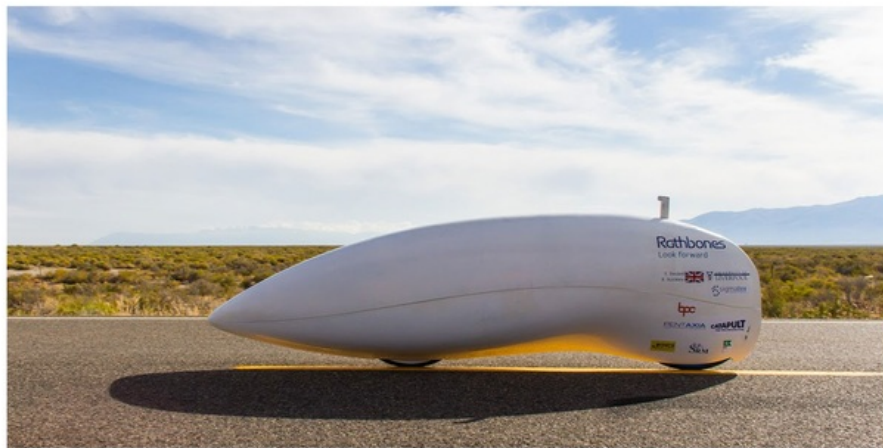
Figure 2.14: University of Liverpool Velocipede Team's entry [17].

The UofL HPV shows a departure from the current accepted shapes. The nose section is quite sharp, departing from the classic laminar flow foils shape used by other teams. They also do not have any wheel fairings external to the shell which had been identified as an inefficient treatment of the wheel to ground area. The team has discussed this and stated that there are no wheel fairings at this time to facilitate development in the wheel wells.

Early testing in the F9c wind-tunnel has identified nose height as a sensitive factor in the generation of downforce. The sharper, low nose of the Team Velocipede HPV may be attempting to manipulate this sensitivity.

Chapter 3

Equipment selection and load calculations

3.1 Windtunnel operation and measurements

3.1.1 Wind tunnel axis terminology

When describing forces and torques within a wind tunnel, the same naming conventions as used for aircraft movement is employed. These are the torques of yaw, pitch & roll as seen in Figure 3.1. There is also the forces of lift, drag and side force. Lift opposes gravity while drag is in the direction of the wind flow.

Roll	Pitch	Yaw
Longitudinal Axis Aileron control	Lateral Axis Elevator Control	Vertical Axis Rudder control
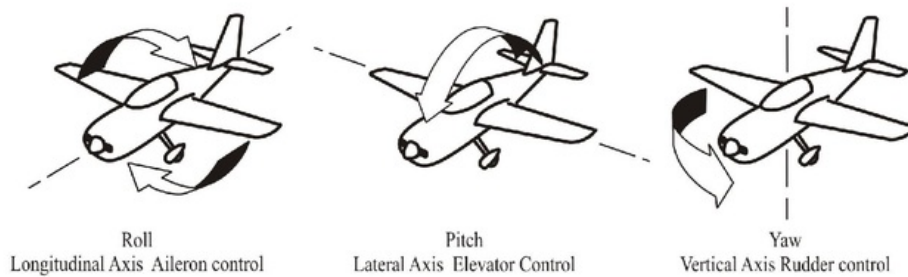
Figure 3.1: The naming of aircraft axes of movement [10]

These same forces and torques apply to the HPV. Of most interest to the HPV is the drag force as any reduction in drag is attributable to a gain in speed. Lift is also monitored as it has an affect on the bike's stability.

3.1.2   Wind speed calculations

The basis for taking measurements inside the wind tunnel is first establishing the wind-speed being generated within the test section. A pitot tube is used to sample the pressure inside the tunnel, seen in Fig. 3.2.
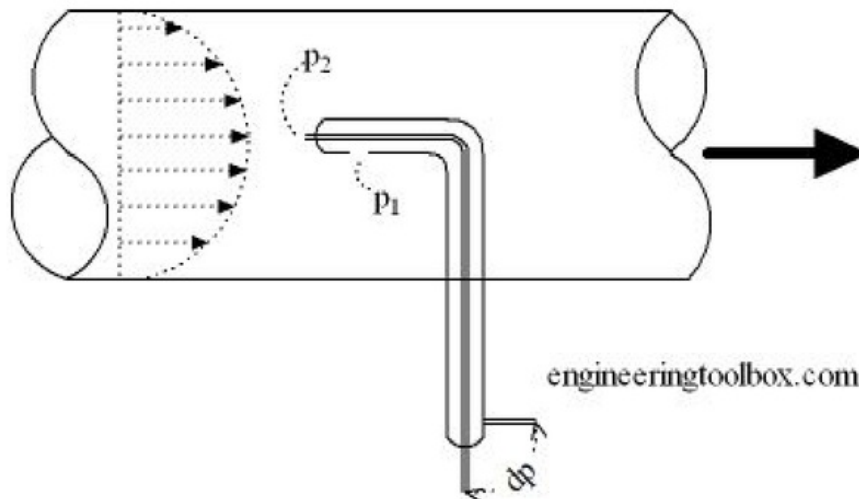
Figure 3.2: Pitot tube sampling air pressure within a wind tunnel [8].

A pitot tube mounted through the walls of the wind tunnel samples the static and dynamic pressure being generated. Equation 3.1 is then used to calculate the velocity in the test section.

$$V_1 = \sqrt{\frac{2 * p_{dyn}}{\rho}} \tag{3.1}$$

Where

V_1	=	Velocity
p_{dyn}	=	Dynamic pressure
ρ	=	Air Density

3.1.3   Wind tunnel control

The calculated wind speed is combined with data on humidity and pressure inside the wind tunnel and is fed into the myRIO data interface. The wind tunnel control program then analyzes the data being received and uses the data to control the revolutions of the motor driven fan to ensure the correct wind speed is maintained within the test section.

The control screen allows the operator to monitor these inputs but the main single control is specifying the desired wind speed in metres per second.

3.2   cRIO & myRIO

The cRIO or CompactRIO and the myRIO are modular controllers used in the operation of the wind tunnel and monitoring the F/T transducer data. Different modules take analogue or digital data and allow the data to be read by the LabVIEW software (Chapter 4) that has been loaded into the controller. The digital and analogue Input/ Output (I/O)
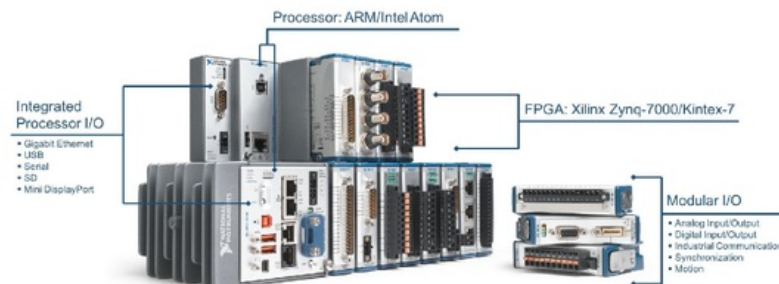
Figure 3.3: The cRIO unit with its modular I/O units [16]

modules can be seen in Fig.3.3 as small plug in blocks in the lower right and these modules are programed with LabVIEW from a computer and the software is stored in flash memory on the module.

3.3   Transducers & sensors

3.3.1   Nano-25 Force/ Torque transducer

Figure 3.4: The Nano25 force torque transducer with the DAQ box

The nano25 Force/ Torque (F/T) transducer is used in conjunction with the ATI Data Acquisition (DAQ) Box to sample the voltage being output by the transducer and passing the information to the cRIO for post-processing by the LabVIEW programs.

Transducer setup and preparation

Technical information on the ATI Nano25 F/T transducer can be seen in Fig.D.2 and D.1. The Nano25 is first run in stationary mode with the QuickCal.vi LabVIEW routine. This routine samples the stationary transducer outputs every 10 milliseconds and averages the voltages to provide a zero setting for the active readings.
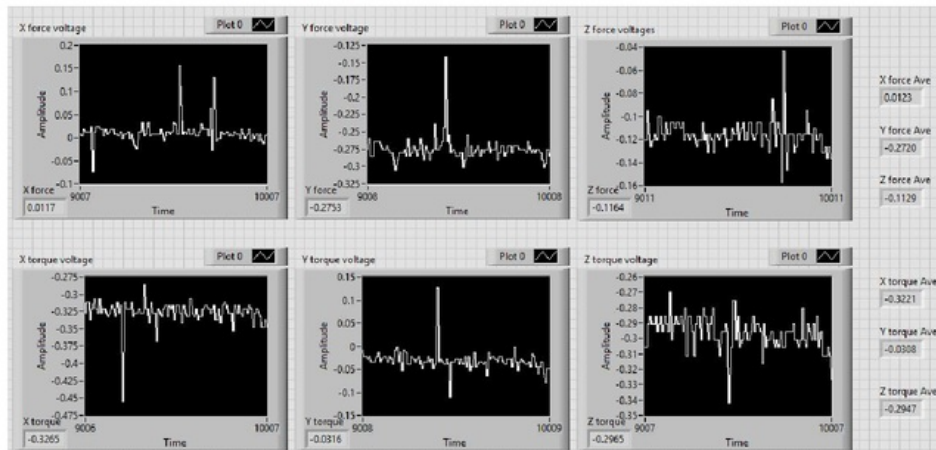
Figure 3.5: Output from the QuickCal.vi routine.

These average voltage values are input into the ForceTorqueAveragingUsingVoltage.vi routine (See Fig. D.5). Once the baseline is set the program is run for 5 sets of data to provide and average to compensate for experimental variation. While the data is being gathered the voltage output is monitored to spot potential errors and the average of the runs is displayed. The output will generally have spikes in the early readings, these spikes are checked to see if they influence or corrupt the data. This is discussed later in LabVIEW, Data Quality.

Once the calibration is completed a range of testing was carried out with certified weights being hung to test the output for the six axes. These outputs were then graphed and a formula for the calibration offset was calculated.

3.3.2   ElectroMagnetic Interference from motor controller

Subsequent to the transducer bench testing and calabration for the force torque transducer, the Nano 25 was placed into the wind tunnel where it was discovered that the Schneider motor control unit was emitting large amounts of ElectroMagnetic Interference

(EMI). This EMI made the transducer unusable in the planned configuration and an investigation into the problem was initiated.

Various methods were attempted to fix the problem but the final solution was to isolate as much as possible the motor controller from the transducer. To achieve this the network cable from the controller was disconnected from the monitoring computer and the emergency stop buttons were re-located from adjacent to the computer. Any unused connections were also removed to lessen their impact.

This achieved a 90% reduction in EMI and allowed the Nano 25 transducer to perform within a reasonable range of confidence. Extra averaging was performed to ensure the highest quality of data was used.

3.4 Bending moments on the sting

Initial estimates of the load on the sting induced by the model in the wind flow were calculated using Eq. 3.2.

$$Drag = C_D * \frac{1}{2}\rho * V^2 * A \qquad (3.2)$$

Where

Drag	=	Drag in Newtons on the model
C_D	=	Drag Coefficient (0.010 used)
ρ	=	Air Density (1.204 Pa)
V	=	Wind Velocity (m/s)
A	=	Reference area (m^2, 0.08 used)
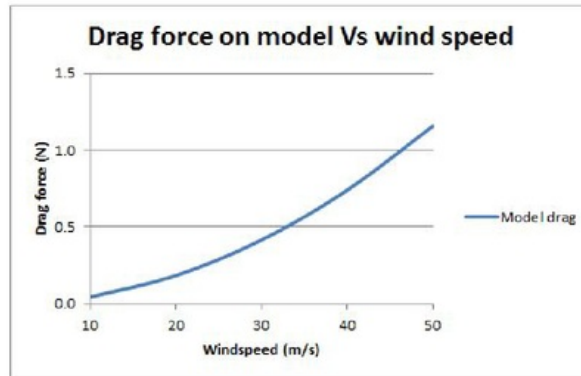
Figure 3.6: Drag force on Model vs wind speed

These drag values are plotted in Fig. 3.6 vs increasing wind speed.

Calculations for the requirements of the sting continued with rough compilation of the weights of the parts as the gravity force was considered to be the greatest loading on the sting. With the combined mass of the test model determined to not exceed 2 kg, the vertical axis of the sting was calculated. An average Modulus of Elasticity of 200 GPa for structural steel was used in the calculations. The maximum expected load from the wind force on the model including a large safety margin was chosen to be 5 N.
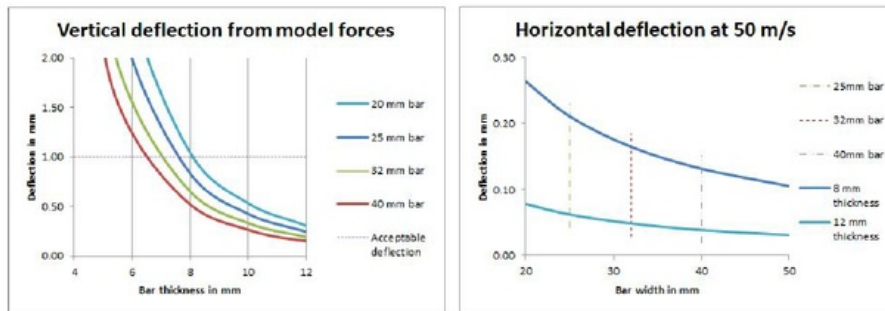
Figure 3.7: Vertical & horizontal deflection of the sting bar given standard size bar options

The vertical deflection was calculated for structural steel bar in industry standard sizes and a maximum allowable deflection of 1 mm was chosen. A range of four standard widths between 20 mm and 40 mm was chosen, with the results graphed in Fig.3.7a. With all four bar sizes meeting the specification for bending resistance once thickness exceeded 6.2 mm, the horizontal bending was calculated.

At the maximum expected wind force of 50 m/s, it can be seen that the horizontal deflection is negligible across all the tested widths and thicknesses (Fig.3.7b). The choice was made to pick the 20 mm * 12 mm structural steel bar for the construction of the sting as it allowed the best option for mounting within the shell while still giving a limit of bending of 0.3 mm vertically and 0.03 mm horizontally at the maximum wind-speed of 50 m/s.

3.5 Transducer mounting considerations

The model mount (Fig.B.1) is where the sting interfaces with the F/T transducer. The mount (Fig.B.2) has an adapter between the sting and F/T transducer to spread the load and allow for finer adjustment of the yaw angle of the model within the wind tunnel. The mount allows ± 5 degrees of adjustment, (Fig.3.9), through the adjustment of the three outer mounting bolts. The centre bolt provides a pivot axis & a cap to the axle and can be left tight.
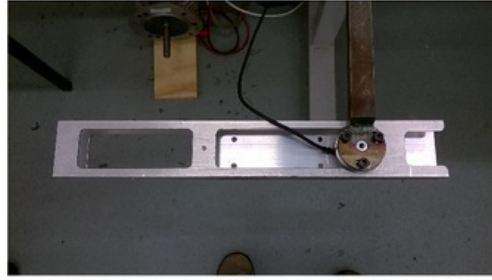
Figure 3.8: Mounting angle normal
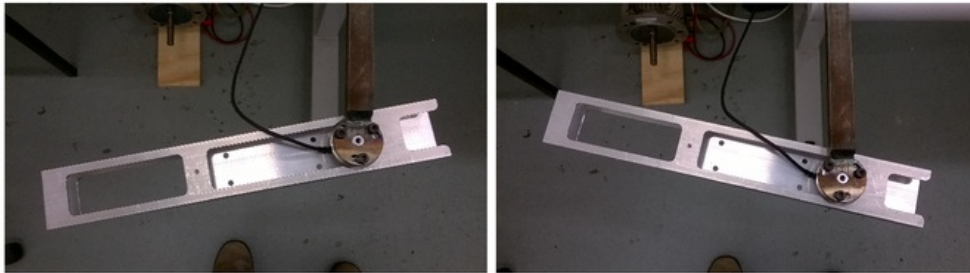
Figure 3.9: Mounting angle extremes

3.6   Selection of the model material

The material chosen for the wind tunnel model was Renshape tooling board, supplied by Meury (*meury.com.au*, [14]) Renshape was recommended by Macquarie University Engineering & Technical Services (METS), who were contracted to mill the shell, as it was an easily milled product with good stability characteristics. Initial estimations of the total volume of the model was between 0.0025 & 0.003 m^3 depending on the amount of material removed internally. This volume was based on calculations obtained from the CREO model but not verified by measurement.

Product Number	Density (g/cm^3)	Shore Hardness ISO 868	Colour
BM 5185	0.47		Apricot
BM 5460	0.70	60-65D	Brown
BM 5172	1.20	80D	Green
BM 5272	1.4	80-85D	Olive

Table 3.1: Details of the Renshape tooling board available, Fig.D.3 [14]

Using the densities above gave a weight range of 1.2 and 4.2 kg. Consideration for the density selection was balancing having a heavier model which would help damped any

small ocsilations against having a lighter model which would impart less static torque in the Y axis whick occurs due to the sting mount being aligned with the estimated Center of Pressure (CofP) rather than the Center of Gravity (CofG). The final decision was to utilize the Renshape BM-8185, as any oscillations could be taken care of with the data averaging.

Part	Left hand side	Right hand side
Nose	91g	92g
Lower mid	156g	156g
Upper mid	141g	140g
Tail	191g	191g
Total	579g	579g

Table 3.2: Individual weight in grams of the base model pieces

With the pieces for the base model weighting 1158g and the chosen BM 5185, this equated to a volume of 2464 cm^3. This is marginally lower that the estimate of 1.2 to 1.4 kg for the use of the BM-8185 and shows that the hollowing internally was effective in reducing overall weight.

Chapter 4

LabVIEW coding

4.1 Data acquisition for Force & Torque

The Nano25 Force & Torque (F/T) transducer as supplied was outputting a noisy signal (Fig.4.1) when operating at the lower end of its specified performance envelope.
To compensate for this signal a LabVIEW routine was written to average out the input in preparation for operation.
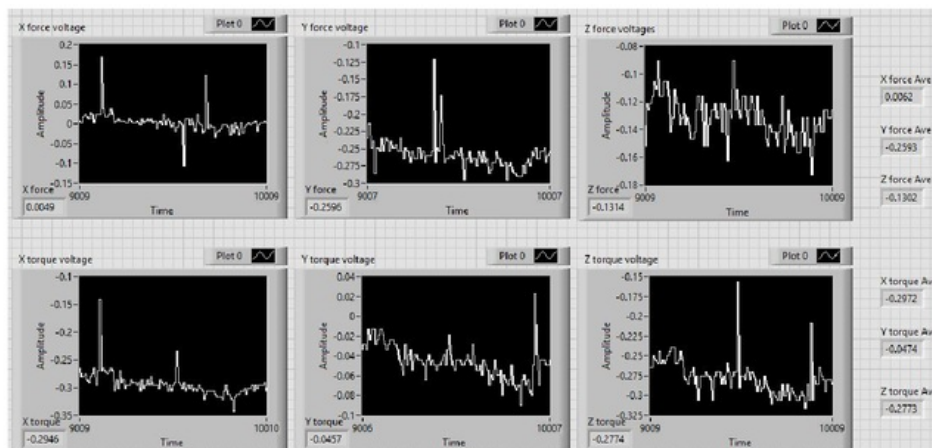
Figure 4.1: Noisy output from the 6 axes of the F/T transducer

This hypothesis was later confirmed as the model was run at higher loads. At these higher loads the signal quality became smoother and the range of output became less.

4.1.1 Calibration routine

The LabVIEW calibration routine samples the voltage output from the 6 axes of the Nano25 every 10 milliseconds and captures 10,000 samples. These captures are then aver-

aged and output to the screen for input into the F/T monitoring program. The QuickCal program also displays a running output of the voltages being samples so large fluctuations can be monitored. This output can be seen in Fig.4.1.

4.1.2   F/T monitoring & data collection

The six voltage offset values from the QuickCal routine are input into the data acquisition (DAQ) program. These offset values are reset for each different configuration tested. Also included in the DAQ program are signal quality readouts to allow the monitoring of data in real time This can be seen as the large readout in the upper left of Fig. 4.2.
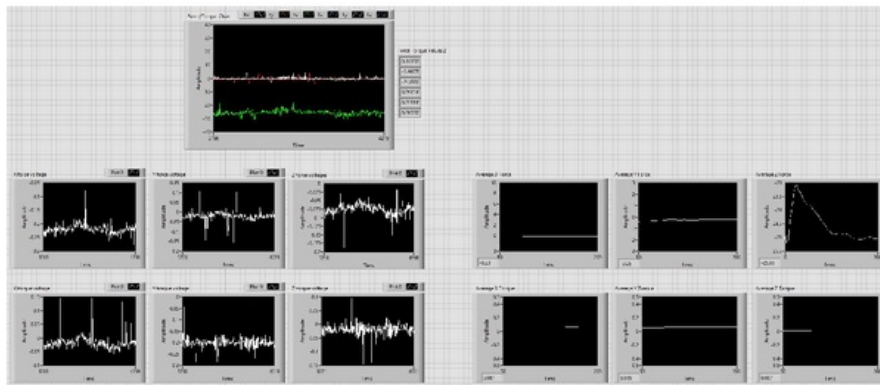
Figure 4.2: Data aquitition from the F/T transducer.

The six readouts in the lower left of Fig. 4.2 are the voltage data being input and the six readouts on the right are the running averages for the six axes.

4.2   Data quality control

As stated earlier, due to the efficiency of the HPV's shape, the model was operating at the lower end of the transducer's performance. This resulted in fluctuations in the data being received and it was identified that the data must be evaluated for quality before being used in results.

Observations of the data being generated during early the calibration & testing phase identified the X axis force as a good indicator of data quality.

Fig. 4.3a shows large fluctuations in the running average towards the end of the run. These fluctuations were part of the experimental variation described above but fluctuations at the end of the run were indications of large variation in input voltage, and thus this data would be discarded. Fig. 4.3b shows the data average converging to a flat line indicating the data was in a similar value range and thus this data would be accepted.
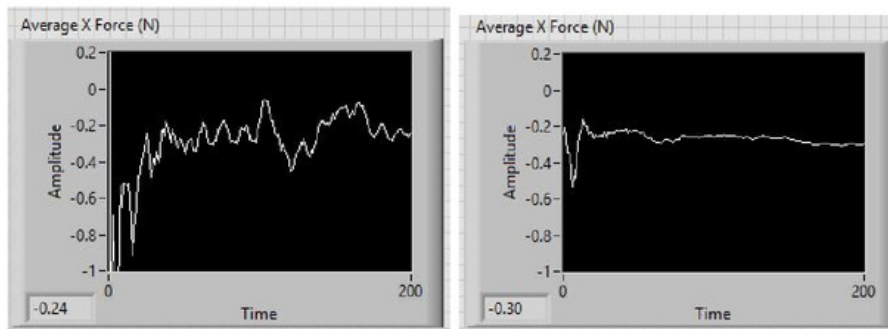
Figure 4.3: Quality of data indications.

Another indicator of quality was the $\pm$ limits. Upon start-up, large fluctuations in the data would often occur, resulting the graph exceeding a range of $\pm$ 0.5 N and this can be seen happening in Fig. 4.3a. This would often give a convergence required and so was not discarded immediately but it was an indicator to pay particular attention to the final data value.

4.3   LabVIEW coding

The LabVIEW coding used in the project can be viewed in larger scale in Fig.D.4 & D.5

Chapter 5

Model Design Parameter Selections

The first objective of the project was to design and construct a reconfigurable wind tunnel test model so that different configurations of nose height & length and different tail heights could be analyzed and the data obtained be used to verify the CFD study that has been ongoing within the MqSpeed Team.
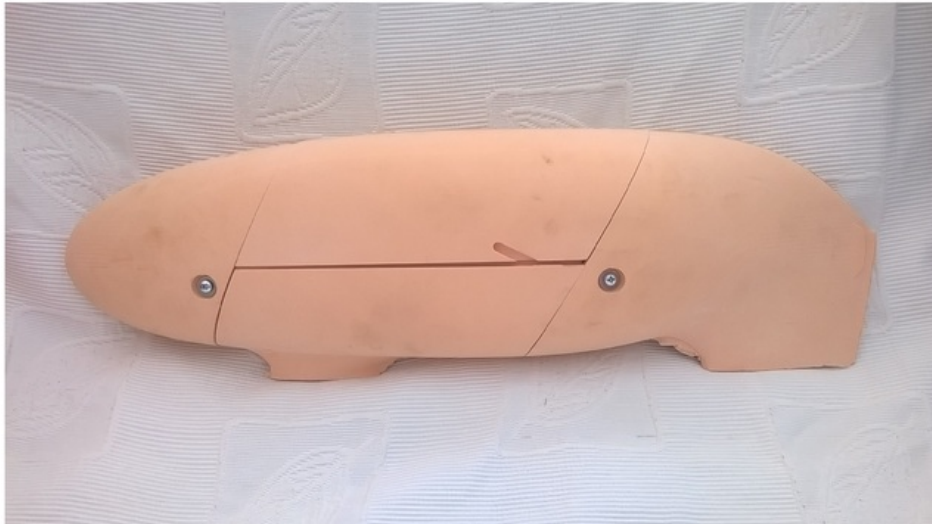
Figure 5.1: The base model assembled and ready for fairing.

These different configurations have been identified as possible sensitive contributors to differing performance of the HPV. The name of each combination configuration is listed in Table 5.1. Each of the pairings in Table 5.1 will be run through the same group of tests multiple times and the data generated will be used in the validation.

By slightly altering the nose height & length and tail heights and testing all the combinations available, the sensitivity of the model to these factors can be explored and

by using this sensitivity, new directions of optimization can be planned.

	Tail Base	Tail +20	Tail +40	Tail +60
Nose Base	Base	Base +20	Base +40	Base +60
Nose High	High +0	High +20	High +40	High +60
Nose Low	Low +0	Low +20	Low +40	Low +60
Nose Long	Long +0	Long +20	Long +40	Long +60

Table 5.1: Model designations

5.1 Previous CFD development

The wind tunnel model is based on Model #34c, developed via CFD for the MqSpeed Team by Sajjad Saleh and others. From this data, the base nose, base tail configuration was selected. This base configuration was then modified as below to give the test configurations.

5.2 The base model

Because these models have been developed solely by means of CFD, with no external validation, this project is needed. The continuing development of the HPV shell can only progress with confidence once the CFD parameters have been validate by wind tunnel data.

This base model (34c) was scaled down to 1:5 scale and had the solidification removed in preparation for the design alterations. 1:5 scale was chosen to keep the model as large as possible without exceeding the maximum 10% tunnel blockage ratio identified [4] as a cause of poor data being produced.

SCALE 1:400
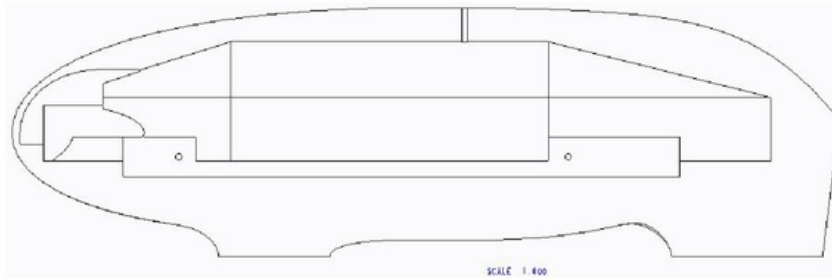
Figure 5.2: CAD drawing of the base model

5.2.1 Model preparation in CREO

Due to a feature of the CREO system, only one solidification action can occur in each model. Because the CAD model is constructed with Boundary Blend surfaces, the normal method of cutting material away from a model can not be used until the final model is complete.

To allow the model to be re-configurable, cut lines were projected onto the surface and these projected lines formed the base for tangential curves to be produced. Having these base curves leave the standard middle section at a tangent is important to ensure that the different nose and tail sections attach with a fair surface needing minimal hand finishing.

5.2.2 Splitting the model

The decision on where to split the model was made with regards to various fixed dimensions of the vehicle and rider. The tail split coincides with the plane from the rider's shoulders and hips. This is a fixed dimension of the HPV and thus any changes to tail configurations would happen behind this plane.

As the model was intended for future experimentation, the nose split was placed with this in mind. When the rolling road mechanism for the wind tunnel is completed, it is planned to have wheels inside the fairing. This requires extra complexity in the model, and so the nose split was located so as the front wheel would stay within the centre section and the nose would be independent of this structure. This meant that the features required for the moving front wheel did not need to be repeated for each nose section tested.

The angle of the nose split was chosen to provide a slight wedge shape to the lid. This wedge locked in the parts when it was tightened down onto the sting, giving a smooth, rigid surface to the model.

5.3 Internal mounts and fittings

As there is a need to install monitoring equipment and to mount the F/T transducer within the model, it had to be hollowed out. The location of the force torque was primarily chosen by the assumed Center of Pressure (CofP), with the Center of Gravity (CofG) as a secondary concern.

The need for this placement was determined from a previous wind tunnel model, which was mounted to balance the model fore and aft. This choice of mounting positions induced an oscillation into the model at higher wind speeds, i.e. over 30 m/s. It was surmised that having the CofP in front of the mounting point caused the nose to be blown slightly to one side with the F/T transducer providing a reaction force returning it to the centre. When this occurred at a high frequency, the oscillation could be easily seen, giving the possibility of false data in the output.

The new mounting point was initially based on Max Munk's Thin Foil Theory [15]. This theory stated that for non-extreme airfoil sections, the CofP will lie at 25% of the
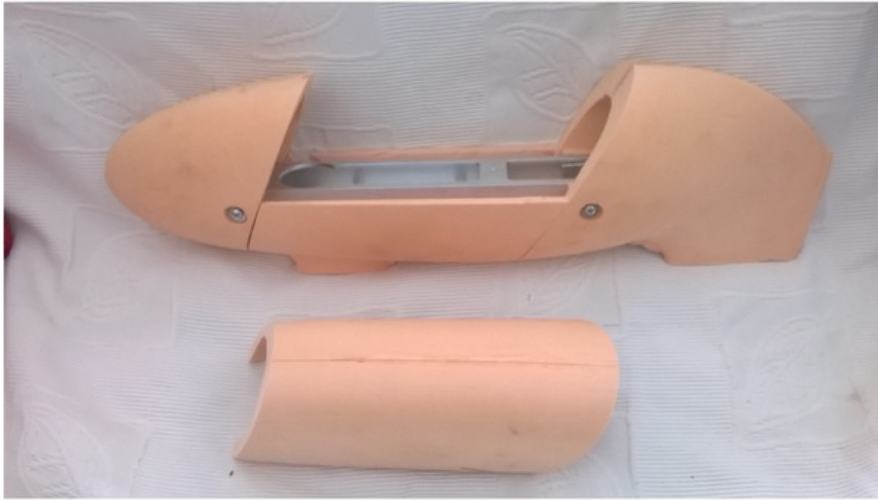
Figure 5.3: The base model with lid removed, showing internal spine.

foil's chord length back from the leading edge. This CofP can and does move around depending on Angle of Attack (AoA) but for the purposes of mounting, this movement is negligible. Provision has been made in each of the nose cavities to place a cylindrical steel counter-weight to help balance the model if deemed necessary.

5.4   Tail Configurations

The base CAD model was sliced at the plane corresponding to the location of the rider's hips and shoulders. While having an angled join in the model increased the difficulty in construction, the area of the HPV from the hips to shoulders is a fixed area of the design so any alterations in the tail would only occur behind this plane. The tail section was also sliced at the mid plane height as the area being tested was specifically the tail height and this allow the rear wheel fairing to remain constant.

The tail height base curve was chosen as a conic arc with a tangent base at the join and a variable angle driven by an exit calculation. The conic arc was chosen so its curve was proportionally reduced as the tail increased in height. This removed the variable associated with changing the curve characteristics and allowed the study to isolate just the tail height and related increase in surface area as the variable under study. The four tail heights are 0 mm from base model, then +20 mm, +40 mm and +60 mm.
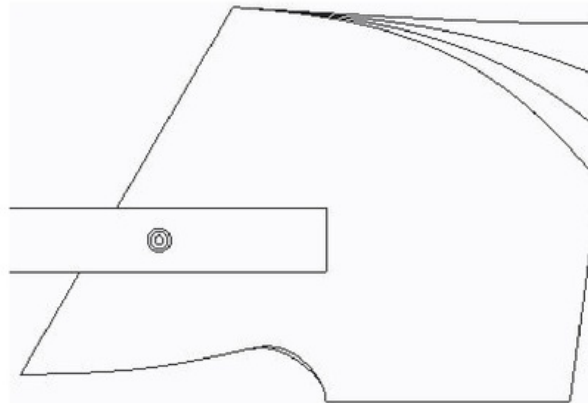
Figure 5.4: The four tail height configurations

5.5 Nose Configurations

The nose section was defined by a plane running from just in front of the front wheel fairing and rising an an angle 15 degrees more vertical than the stern slice plane. This was done to give the middle hatch some relief as it was removed while ensuring a tight and secure fit while operating in the wind tunnel.
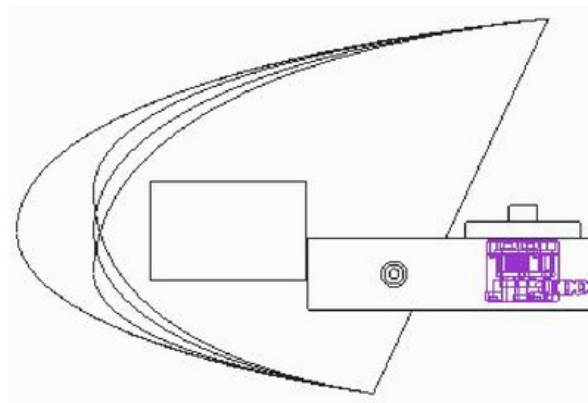
Figure 5.5: The base nose with the 3 option noses superimposed.

The nose section was also based on conic arcs for the same reasons of repeatability of curvature needed in the tail section. The construction of the conic was simpler in the nose as all the curves could have tangents at each end and the section was also fitting to a straight cut. This made the nose section more robust in relation the the changes that could be made without the model crashing. The chosen nose test options are shown in

Fig.5.5 superimposed on one another. The four noses are base, ± 15 mm in height and $+27$ mm in length. As nose height had been identified as a critical dimension in drag and surface area was secondary, it was chosen to make the chance in nose length greater than the change to nose height to highlight the differences more readily.

5.6   Construction errors

Construction of the model was outsourced to the team at METS for milling on their CNC router. Unfamiliarity with three dimensional milling resulted in some errors during construction, requiring hand finishing to the model parts.

These errors also resulted in a lack of material to complete the full set of test parts. This meant that the low nose and the 20 mm high tail were not constructed.

As mentioned in Section 7.2 Continuing work, the low nose part will be required to fully explore the downforce generated by the model.

Chapter 6

Testing, Results & Discussion

All data in the following graphs have been converted to non-dimensional coefficients where applicable and unless otherwise stated. The reference values used are stated in Table 6.1.

	Dimension	Reference value
Force	Reference Area	0.08 m^2
	Velocity	25 m/s
	Air Density (ρ)	1.204 kg/m^3
Torque	Reference length	0.35 m

Table 6.1: Reference values for coefficients

6.1 Force & Torque

6.1.1 Testing parameters and axis naming

Because of the low C_d of the test models and the small scale involved, the testing has been conducted at high wind speeds. Initial testing of the model set an upper stable wind-speed limit of 25 m/s, or 90 km/h, before the model developed low vibrations and possible skewed results. The conversions used are shown in Table 6.2, and the motor was manually set at 24.9 Hz.

Axis naming

In this document the names of the three force axes and the three torque axes have been replaced with motor racing terminology. Force X is termed drag and is positive for increasing drag. Force Y is termed side-force and is positive moving towards the viewing window of the wind-tunnel, towards the left looking into the tunnel. Alternatively, negative side-force indicated movement towards the mounting window or sting side. Force Z is gravity and is positive downwards. Downforce is torque Y and is positive for a

Motor revolutions (Hz)	Windspeed (m/s)	Windspeed (km/h)
10.6	10	36
15.3	15	54
19.9	20	72
24.9	25	90
27.6	28	101
29.7	30	108
32.2	33	119
34.1	35	126
38.0	39	140

Table 6.2: Windspeed to motor revolutions, obtained experimentally

downwards torque, therefore increasing numbers indicate more force downwards. Yaw is the Z torque and is positive for clockwise rotation looking down on the tunnel.

6.1.2   Nose configuration data with zero AoA

Each test session was conducted over a single day. The three noses were tested three times each in sequential order to ensure each test run shared similar conditions. The sequential order for each test session was changed so each nose had a different order in the testing lineup.

Each individual run consists of running the LabVIEW data collection routine in Fig.D.5. This routine sampled the F/T output 20 times at 25 millisecond intervals and averaged 200 of these samples to give a run result.
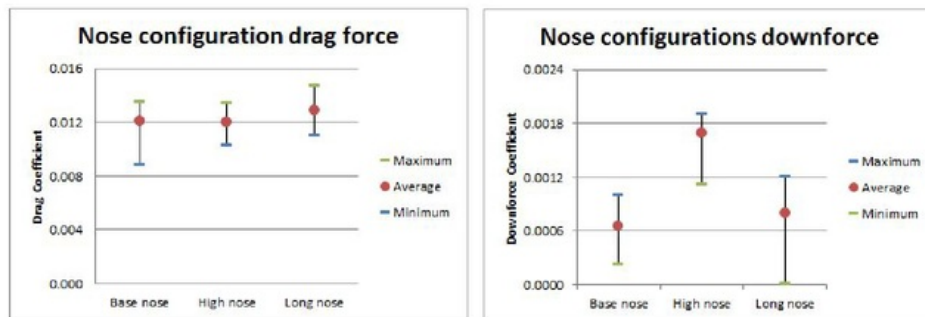
Figure 6.1: Nose configuration data, Zero AoA

The drag force shown in Fig. 6.1a indicates values of a range to be expected. Both the base nose and the high nose are showing similar drag amounts as their total surface area is the same. The long nose, with its higher surface area, is shown to have a higher drag

factor. All three noses use proportionally the same curvature and thus the aerodynamic influence is in the same range.

During the testing of downforce of the nose configurations, the higher downforce value for the high nose was initially unexpected, although with further research it was recognized that the higher nose was presenting an inverted wing shape to the airflow. This characteristic will be an important factor in tuning future shell shapes for the HPV team as the downforce will be able to be altered without increasing the drag associated with the change.

6.1.3 Tail configuration data with zero AoA

Early testing of the nose configurations indicated that the resolution of the test data would be too small to identify the differences in the four tail sections, so the tail configuration testing was initially run using the base tail and the + 60mm tail. The tests were run using the same data acquisition routines and the tails were alternated each test so that they were tested in similar conditions over the two days of testing.

The data in Fig.6.2b is showing a proportionally large range in values. It is thought that with the model operating at speeds approaching its unstable region that slight vibrations have a greater effect on the downforce values as the vibrations can be proportionally higher than with the larger drag values.
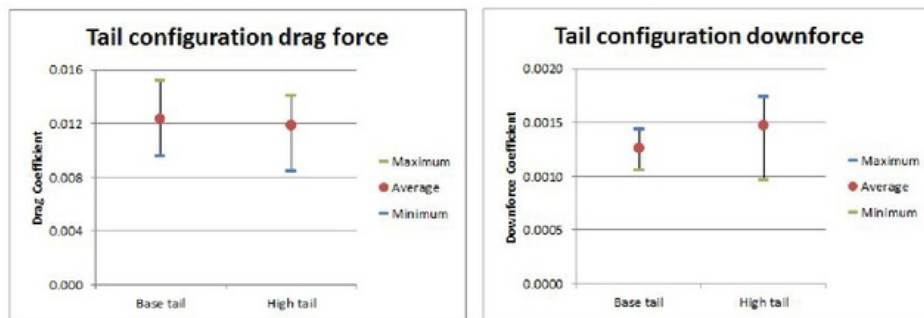
Figure 6.2: Tail configuration data, Zero AoA

The plan-form shape of the tails is the same and so the height of the tail should not have a significant effect on the downforce being generated. The small increase in volume of the + 60mm tail explains the slightly higher downforce being produced but the major contributor to differences in downforce can be attributed to the nose shaping. The large percentage range of values as a could be further examined but if the values are taken in actual force, it can be seen that the range of values is ± 0.01 N, and can thus be considered negligible and within the variation explained by experimental error.

6.2   F/T testing with Angle of Attack introduced

6.2.1   Side force and drag with AoA

	Nose section		Tail Section
Test Config. 1	Base nose	&	Base tail
Test Config. 2	Long nose	&	Base tail
Test Config. 3	Long nose	&	High tail
Test Config. 4	Base nose	&	High tail

Table 6.3: Configuration order for Yaw testing

The model was run at Angles of Attack of 0.5, 1.5, 3 and 5 degrees, utilizing the base & long noses and the base & + 60mm tail sections. The order of configurations to be tested are shown in Table 6.3. When setting up the model, 0.5, 1.5, 3 & 5 degrees corresponds to 3, 9.5, 19 and 31mm sideways offset at the tail from the tunnel centerline.

When considering the yaw angle in relation to the full size HPV it is worth noting that, when traveling at the current operating speed of 140 km/h, to get a wind angle 5 degrees off the nose would require a 12.2 km/h side wind and time trials are canceled when the wind-speed reaches 6 km/h. Testing beyond 5 degrees represents a factor of double allowable wind speed and is therefore is considered interesting but not necessary.
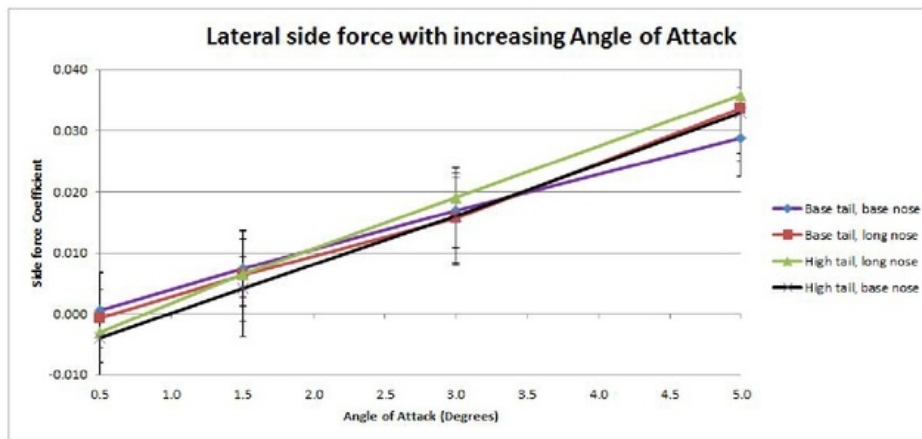
Figure 6.3: Plot of side force for increasing AoA

The side-force data depicted in Fig.6.3 shown an approximately linear increase in side force for all configurations as Angle of Attack increases. This is to be expected as the side-force is a function of the area being exposed to the passing air flow combined with the aerodynamic forces introduced as asymmetry starts to occur with the airfoil shape of

the HPV. These aerodynamic forces being seen as an increase in the Yaw torque (Fig.6.6). This linearity will give a predictability to the loading, which is desirable considering the negative effects of the yaw torque discussed later.

It can be noted that all the configurations have a negative value associated with it at the beginning of the graph. This minor but measurable negative force is thought to be caused by the asymmetry in airflow caused by the sting. The different configurations need between half and one degree of positive AoA to negate the effect of the sting.
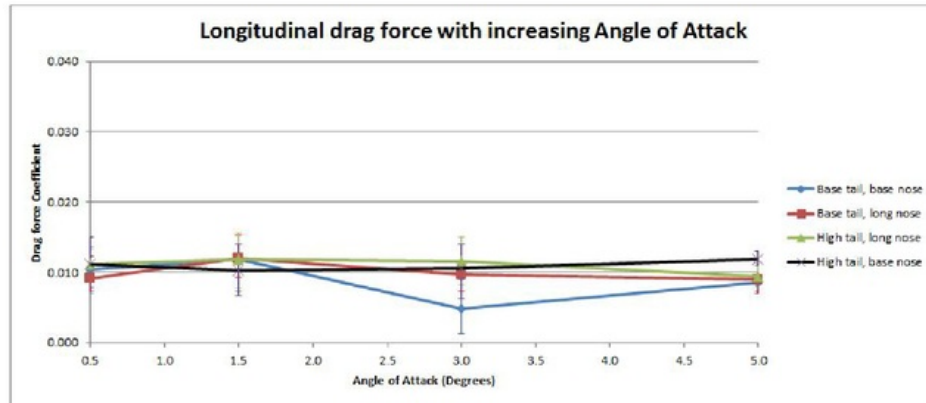
Figure 6.4: Plot of drag force for increasing AoA

The increasing side-force is matched with a decrease in drag as the F/T transducer is aligned with the model and as the Angle of Attack increases there is a reduction in longitudinal air flow. The drag force is not reducing in direct relation to the side-force and so the shell sees a net increase in drag as the Angle of Attack increases.

Of interest in Fig. 6.4 is that all configurations exhibit an increase in drag as soon as the AoA is increased. Also of note is that both base nose configurations are showing a trend towards increasing drag past 5° AoA. It is not expected that this increase would continue with further rotation but is stands as an area for further exploration as the two long nose configurations show the expected decrease in drag with increasing AoA.

6.2.2 Downforce and Yaw torques with AoA

The downforce coefficient data plotted in Fig. 6.5 shows increasing positive values as increasing downwards rotation, and is a torque force measured around the transducer mount. The plots show both long nose configurations as having less downforce than the base nose configurations. It is reasonable to expect that the long nose configurations would have their Centre of Pressure further from the transducer mount because the airfoil shape is effectively shifted forward by the longer nose. This would indicate that the plot in Fig. 6.5 is under representing the difference in actual downforce being produced.
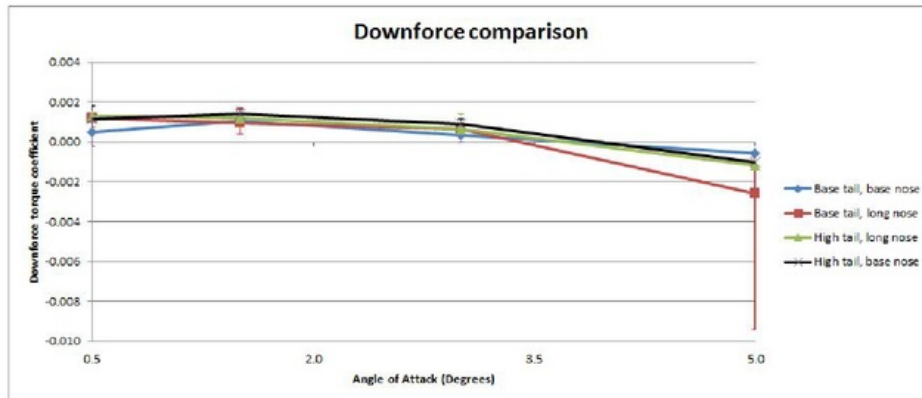
Figure 6.5: Comparison of the downforce generated with increasing AoA

It is also worth comparing the downforce data with no AoA presented in Fig. 6.1 with the downforce generated with increasing AoA shown in Fig. 6.5. With zero AoA the base nose and long nose generate similar amounts of downforce and the high nose generates more downforce for the same drag and the base nose configuration. When the AoA is increased, the high tail looses downforce much quicker that the base tail, indicating that while the high tail reduces the unwanted yaw force, the downforce is reduced as well. Once again, the range of downforce from maximum to minimum of any configuration is 0.04 Nm and this difference is unlikely to create instability in the handling of the HPV.
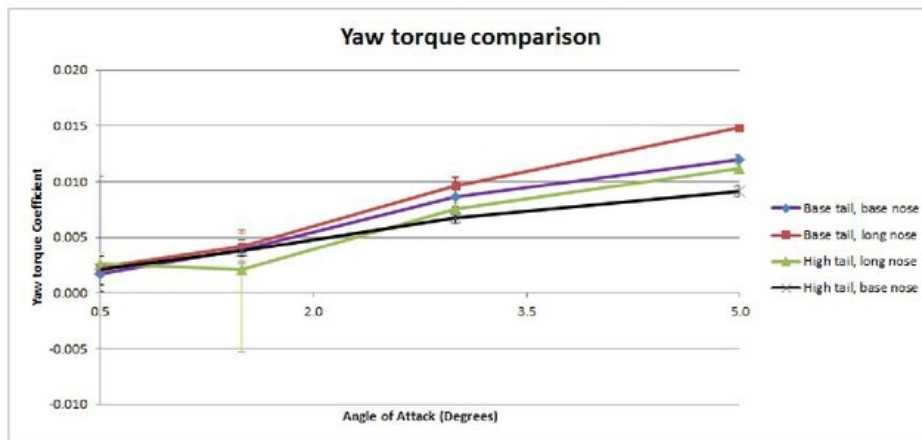
Figure 6.6: Comparison of yaw torque with increasing AoA

The information plotted in Fig. 6.6 is of great importance to the MQSpeed Team and

the data generated was unexpected. The plot shows an increasing tendency for the HPV to turn away from the wind with an increase in AoA. This characteristic is of concern because it shown a reinforcing of the force turning the vehicle away from the wind rather than a correcting force that helps straighten the vehicle.

The data shows that both high tail configurations have less torque acting about the transducer mount and that the high tail, base nose gives the least torque values. The high tail is generating a partial correction moment, not enough to cancel out the torque but moderating the amount the bike is forced to bear away.

Because the HPV has a limited angle of steering available to correct it's direction, it is possible that the yaw torque described will be more than the rider can compensate for. It has been indicated above that 5° of AoA is considered an extreme occurrence given the competition rules on external wind-speed but this yaw torque should be kept in mind when testing outside of competition where the wind angle is not carefully monitored.

To properly evaluate this tendency to drive away from the wind with increasing AoA needs the actual Center of Pressure to be calculated. Hand calculations were attempted but a CFD study will be more useful in determining the centre.

6.2.3 Validation for reverse angle

As the model is asymmetrical in nature in relation to the sting being attached to the far side of the model, a short validation test was conducted to ensure reverse angle values were in a similar range to the angles tested. Because of structural constraints in the model, the maximum reverse angle that could be tested was 3.9 degrees, or ±25 mm of tail offset.

	Shell Drag	Sideforce	Downforce	Shell Yaw
+3.9°	0.31	0.70	-0.001	-0.113
	0.26	0.75	-0.001	-0.111
	0.27	0.69	0.000	-0.115
	0.27	0.70	-0.002	-0.114
	0.32	0.78	-0.001	-0.115
Average	0.286 N	0.724 N	-0.0010 Nm	0.1136 Nm
Range	0.06 N	0.09 N	0.002 Nm	0.004 Nm
−3.9°	0.28	-1.120	-0.001	0.080
	0.33	-1.06	-0.001	0.079
	0.33	-1.08	-0.001	0.082
	0.37	-0.98	0.000	0.082
	0.32	-1.03	0.000	0.085
Average	0.326 N	1.054 N	0.0006 Nm	0.0816 Nm
Range	0.09 N	0.14 N	0.001 Nm	0.006 Nm

Table 6.4: Reverse angle comparison with Base Tail & Base Nose

In Table 6.4 the positive angle corresponds to the angle all the previous tests were

carried out and indicates the tail moving towards the sting side of the model. The negative angle corresponds to the tail moving away from the sting side.

While reduction of wind disturbance was paramount in the design of the sting fairing, the efficiency of the HPV model meant that percentage wise, the sting still produced a small asymmetry in the air flow around the test model. This difference is most telling when comparing the drag value for the shell at both extremes of rotation.

With the sting on the windward side of the model, the data shows a lower drag value than when the sting in on the downwind side of the model, in the region of 0.04 N when the averages are considered. As a percentage of the overall value this is small but it was consistently measured and so included in the report.

All of the yaw testing was conducted with the sting on the windward side so is is expected that the values obtained will be closer to the actual HPV shell as the sting will not be attached in full size. The addition of extra drag can be compensated for when continuing CDF studies are undertaken.

These results also correspond to the findings in "Yaw force with increasing AoA" where an AoA of between half and one degree was needed to overcome the effect of the sting, depending on the configuration being tested..

6.3   Drag at over benchmark windspeeds

Early on in the setup phase, the wind tunnel models were tested for stability so as to obtain valid data in a consistent environment. When the models were tested at more than 25 m/s there were occasional tremors in the model and thus the test speed of 25 m/s was established as the benchmark wind-speed level. It was always the expectation that once the regular testing was completed, the model would be tested at wind-speeds over the established benchmark.
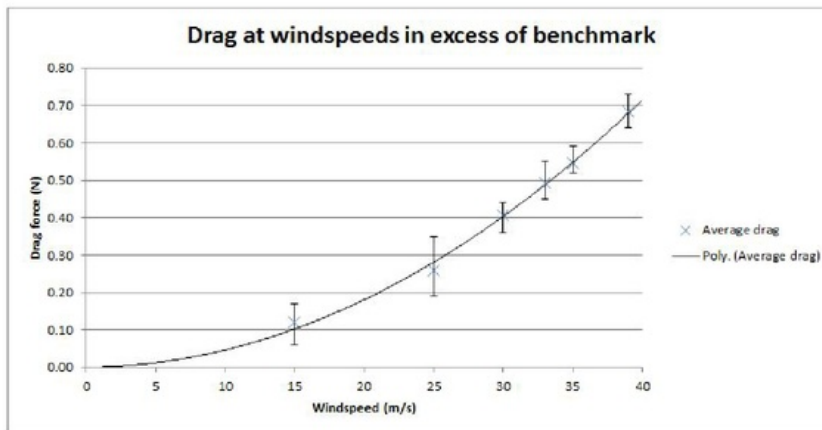
Figure 6.7: Results for over-speed testing

Once testing was continued past the benchmark speed, the tremors were apparent but short lasting and were mainly small harmonic frequency type shudders. These tremors didn't effect the data being obtained as had been expected, but they had to be carefully monitored in case the resonance multiplied. The data obtained at the higher wind speeds showed less range between maximum and minimum readings and the average shows a consistent progression as the speed increases.

The tightening up of the range with higher wind-speed force being applied shows an increasing validation of the proposition that the transducer was operating at the low end of its spectrum, even though the literature did not indicate this. This can be seen in Fig. 6.8, where the range shows a marked decrease with increasing wind-speed when converted to a coefficient. Use of a transducer with a lower operating range should therefore provide higher quality data in future experiments.
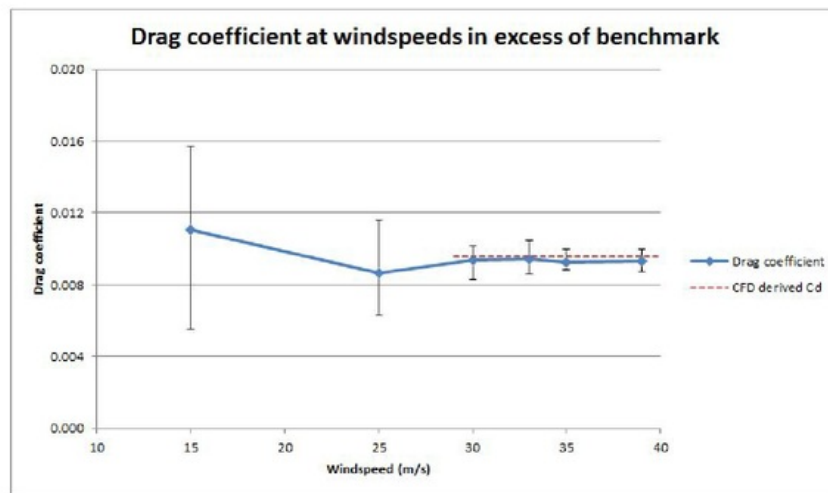
Figure 6.8: Higher wind-speed drag converted to Coefficient of drag (C_D)

Also interesting in Fig. 6.8 is that at higher speeds, the measured C_D is averaging 0.0094. This can be considered a valid result as the CFD study resulted in a C_D of 0.0096, values within 2% of each other. Further testing should be attempted at these higher speeds to fully validate the CFD study.

With an expanded experiment program in the future, the forces and torques at these higher wind-speeds can be explored further and with greater accuracy in the data obtained.

Chapter 7

Conclusions and Continuing Work

7.1 Conclusions

7.1.1 The Model

The wind tunnel model as originally conceived and constructed has been highly successful. It has come through a rigorous testing program in excellent condition and has proved to be easily adjustable for the various configurations and angles of attack. The internal mounts have lasted longer than expected with their screw attachment still being in sound condition. The addition of helicoil inserts will prolong it's lifespan even further.

7.1.2 Hardware and Software

The discovery of the EM interference from the motor controller was unexpected but was able to be resolved through both isolation of the controller from the transducer and with software data filtering means. This EMI needs further investigation as it complicated operation of the tunnel and creates errors if not monitored.

The operation of the F/T transducer was also not as straight forward as originally expected. The transducer had never been properly validated & calibrated in it's operating environment and this added complexity to the project. The validation & calibration was able to be carried out in parallel with the design phase and thus only added 5 - 7 days to the early portion of the project.

Developing the DAQ software with LabVIEW was straight forward as it is the exact situation the program was designed to perform. Integration of the calibration/ zeroing program with the DAQ program will deliver small improvements but it is not necessary for future continuation of the project.

7.1.3   Conclusions from testing

Drag & Sideforce

The average C_D of the model with zero AoA was calculated to be 0.0122. The base nose, base tail configuration that the CFD results are base on produced a C_D of 0.0121, with the CFD calculated C_D of 0.0096 being approximately 20 % less. It is worth remembering that the CFD C_D was obtained at higher wind-speeds and it has been shown that the C_D changed with wind-speed.

The drag coefficients for the different nose sections increased in relation to their surface area increase. There were small differences between tail sections but these again were related to increases in surface area.

All configurations showed a slight increase in drag when AoA was introduced with longitudinal drag then decreasing as the airflow became more side-on. The increase in AoA produced a consistently linear increase in sideforce.

Better CFD validation occurred at higher test speeds. When the model was tested at 30 m/s and higher, the measured C_D averaged 0.0094. This represents a difference of less that 2% against the data produced by CFD. The data also exhibited less range in values, indicating the transducer was operating in a better area of its performance envelope and thus, more accurate data was being sampled. Further testing at high speed will be needed for full validation.

As the HPV was highly developed in CFD to optimize its drag profile, it is difficult to make recommendations with regard to improving the drag, only comments on validation of the CFD model are applicable in this section.

Downforce

The downforce being generated by the shell is low in comparison with the weight of the HPV. The downforce maximum of 0.018 Nm and the maximum lifting torque of 0.027 Nm are not enough to seriously endanger the rider, but the handling characteristics can be altered with different configurations.

The high nose developed the most downforce while having the same drag as the base nose. This would indicate that the downforce of the HPV can be tuned for specific handling characteristics without affecting the overall drag of the shell. Further experimentation with a low nose will confirm if this is the case.

Earlier simulations by the team indicated a negative impact on stability associated with the decrease of downforce but increasing downforce has a negative impact on rolling resistance. By adjusting the nose height for different expected load cases, these handling characteristics can be optimized.

Yaw

The MqSpeed HVP shell has been optimized with CFD purely with regard to reducing drag on the shell. With the wind tunnel model able to rotate up to 5°, it was possible

to look into drag changes under increasing AoA. The data obtained shows an increasing torque load away from the wind with increasing AoA. This torque could have negative implications on the handling of the HPV and in extreme cases, could become a safety issue.

Further study needs to be carried out such as moving the sting mount further forwards to the center of pressure of the angled model. CFD modeling will be needed to accurately locate the CofP in this angled case but this information will help develop a safer HPV.

Continuing CFD studies, with AoA included, can investigate the slight net drop in drag at small AoA in certain configurations and see if this trait can be utilized for further drag reduction.

7.2   Continuing work

Due to milling errors while the model was being machined by outside contractors, the fourth nose (low nose) was unable to be produced. Because the high nose showed similar drag data to the base nose but with much higher downforce being generated, continuing study should include this low nose to see if negative downforce (lift) can be generated. While lift is not necessarily needed or wanted, knowing the effect nose height has on downforce will play an important factor in tuning the shell characteristics.

Another factor that can have a big influence and is worthy of continuing study is the effect tunnel blockage has on data generated. Further investigation of tunnel blockage will determine how big a model can be. Any increase in the allowable size of the model will increase the resolution available for the data and increase the number of configurations that can be tested.

A continuing CFD & wind tunnel study will need to be conducted into developing a shell that exhibits a correction tendency to increasing AoA. This should make for a more efficient HPV as the required steering angle can be reduced and will give an added safety factor to the pilot.

When the next round of research is begun the initial shell will have been constructed & tested by the MqSpeed team. This first shell will also generate questions to be answered by CFD and wind tunnel testing to facilitate further development.

The PIV portion of the study was not undertaken. Conducting the PIV study will enable further development of the HPV shell in relation to the wake being generated.

Chapter 8

Abbreviations

AoA	Angle of Attack
BM	Battle Mountain, Nevada. Site of the annual HPV world record attempt
CAD	Computer Aided Design
CAM	Computer Aided Manufacture
CFD	Computational Fluid Dynamics
CNC	Computer Numerical Control
CofG	Centre of Gravity
CofP	Centre of Pressure
CREO	Suite of CAD software from PTC
DAQ	Data Acquisition
DELFT	Delft University of Technology, Netherlands
EMI	ElectroMagnetic Interference
F/T	Force/ Torque
FEA	Finite Element Analysis
HPV	Human Powered Vehicle
IHPVA	International Human Powered Vehicle Association
METS	Macquarie University Engineering & Technical Services
MqSpeed	Macquarie University Human Powered Vehicle Team
PIV	Particle Image Velocimetry
WHPSC	World Human Powered Speed Challenge
UAV	Unmanned Aerial Vehicle
UofL	University of Liverpool
UofT	University of Toronto

Appendix A

PIV training and testing

A.1   Overview

Because of the nature and power of the laser being used for the PIV experiments, specialised training and some medical (eyesight) tests must be performed. The following section details the testing and training undertaken before the PIV experiments could take place.

A.2   Documents relating to PIV training

The specified training and induction was completed during the course of the project and information relating to this qualification is on record with:-

Dr Susan Law
Macquarie University Engineering Dept.
E6A 241.

A.3   Documents relating to PIV medical testing

Faculty of Science

MACQUARIE University
SYDNEY·AUSTRALIA

Appendix XIII – Laser Operator Examination Form
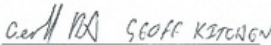
	Yes	No
10. Ophthalmoscopy normal?		
If No, describe: R & L temporal peripheral retina tiny	☐	☑
Photograph if necessary dot haemorrhages , OPTOS		
scans taken.		

11.   Other examinations

12.   Summary and Comment

All findings within normal variation.

Helen Yin.   23.9.2016

Optometrist: Date
(Print and Sign)

Geoff GEOFF KITCHEN   23/9/16

Patient   Date
(Print and Sign)

NB: The current fee (1/1/10) is S90 and includes photographs of the patient's retinas.
As of 1/1/2015, OPSM will invoice the University directly.
Please return your exam report to Dr Susan Law (x8126, E7B-251)

31st August 2015   Page 4 of 4

Figure A.1: Eye exam signoff

Appendix B

Manufacturing Drawings

B.1 Overview of manufacturing drawings

The manufacturing drawings to follow are:

1. Main spine

2. FT transducer top mount

3. Sting end

4. Sting

5. Sting fairing

B.1.1   Main spine

B.1.2 FT transducer mount

Figure B.1: Milled steel connector for the sting

B.1.3   Sting end

Figure B.2: The mounting adapter for the F/T transducer
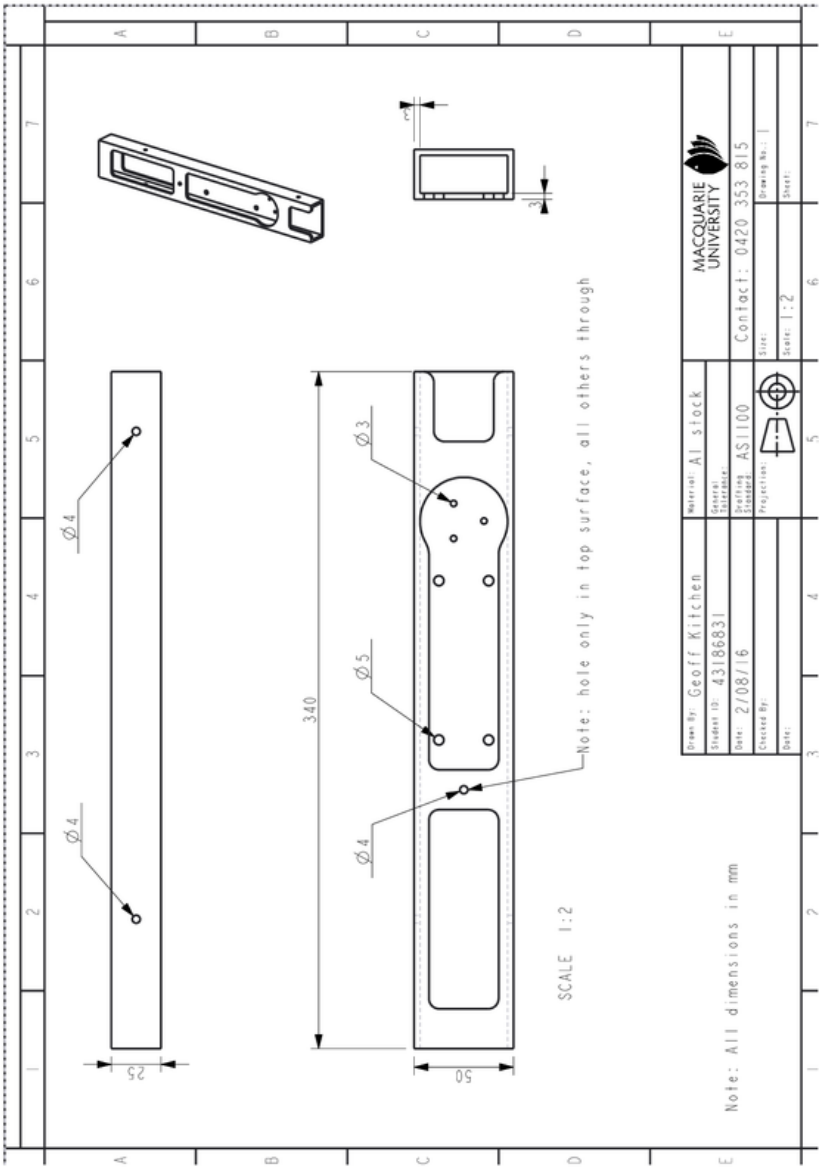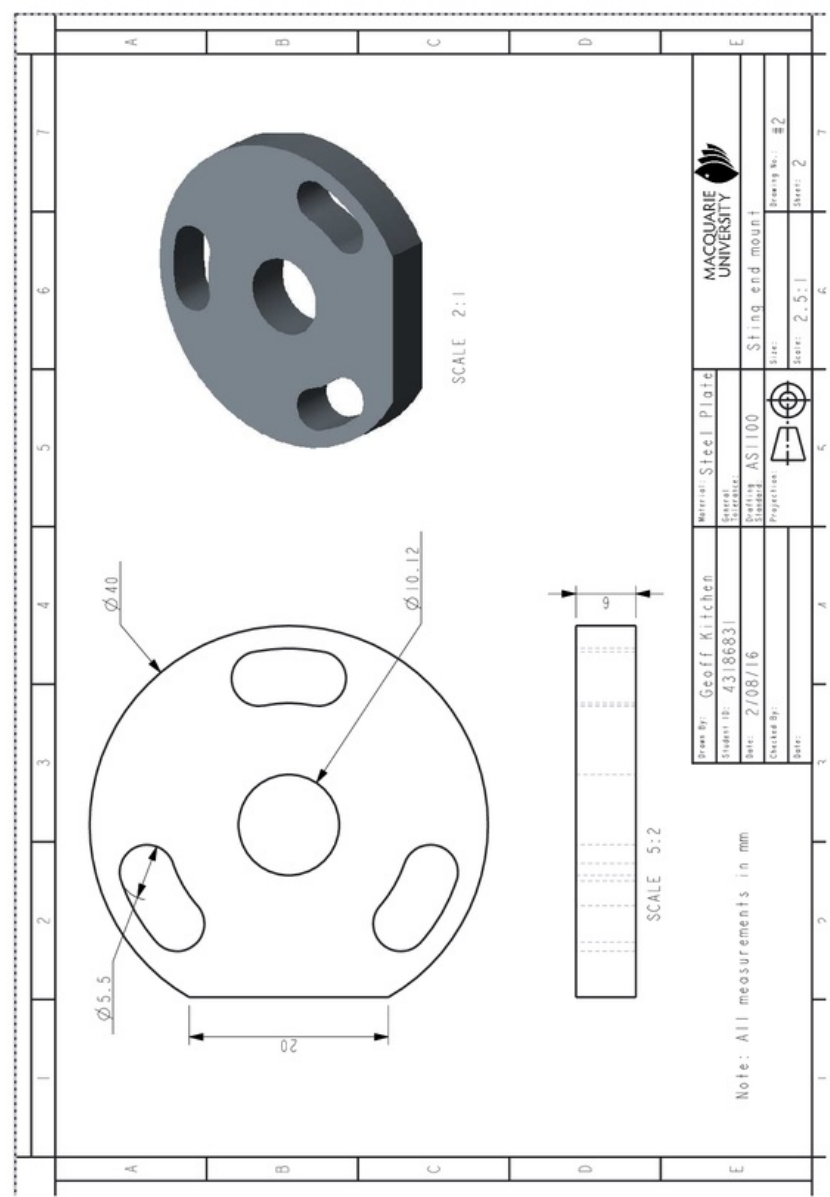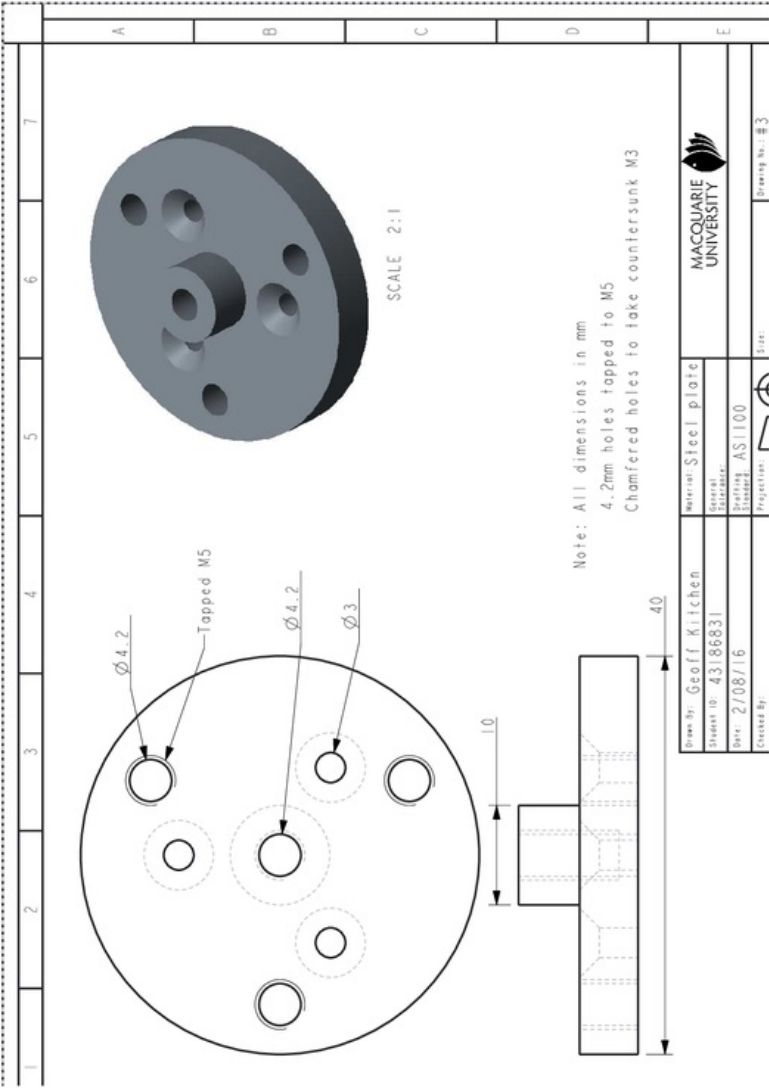
B.1.4   Sting
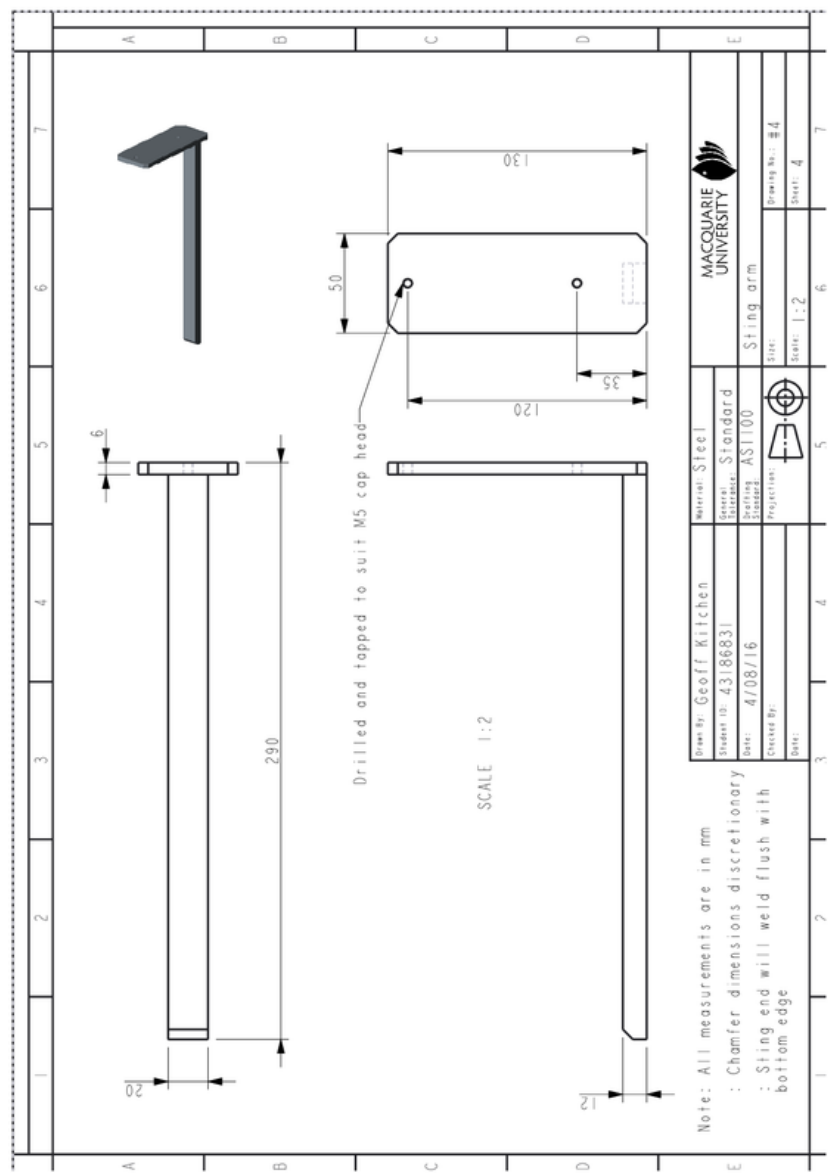
Figure B.3: The assembled sting

B.1.5   Sting fairing
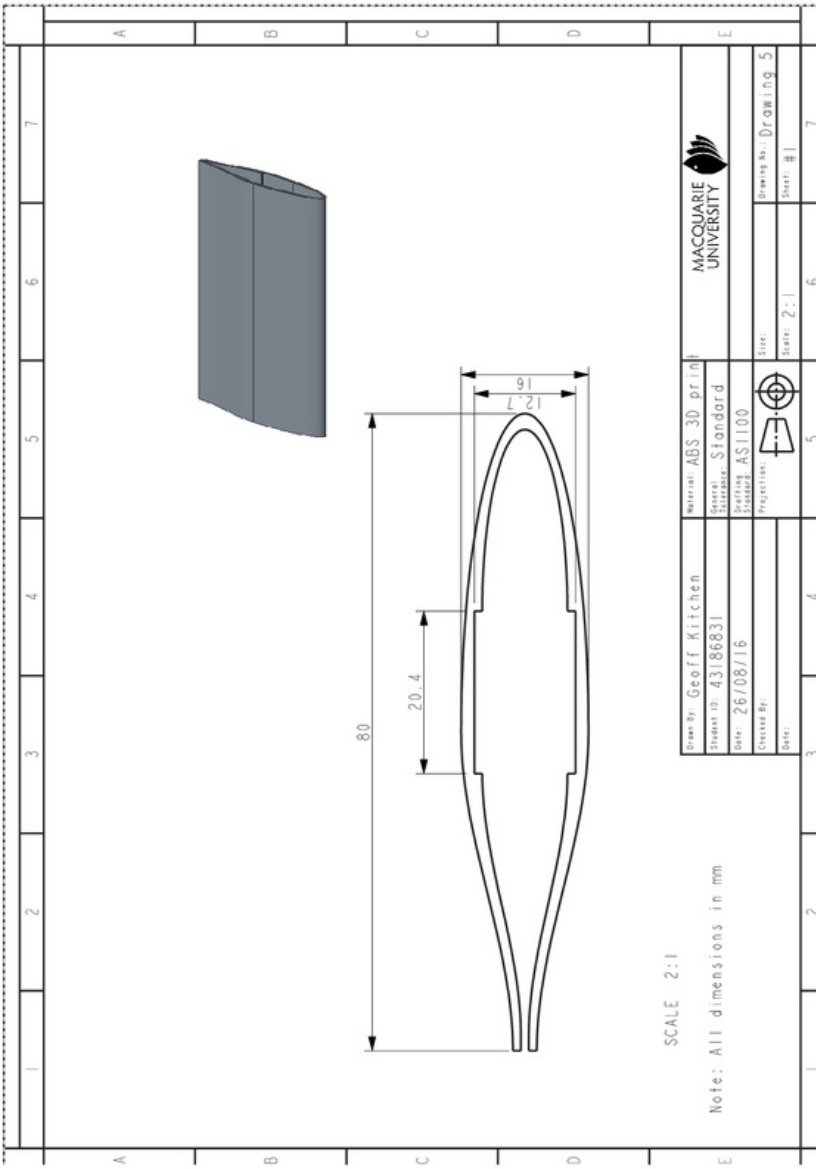
Figure B.4: 3D printd fairing for the sting

B.2   Diagrams

The diagrams following show:

1. Nose layout

2. Tail layout

3. Base model

Appendix C

Raw data

C.1 Zero AoA data

C.1.1 Nose configurations

		Drag	Downforce	Yaw
Test 1	Run 1	-0.266	-0.0074	0.0122
	Run 2	-0.360	-0.0072	0.0024
	Run 3	-0.356	-0.0062	-0.0024
Test 2	Run 1	-0.362	-0.0106	0.0094
	Run 2	-0.408	-0.0102	0.0100
	Run 3	-0.368	-0.0070	0.0014
Test 3	Run 1	-0.386	-0.0072	0.0034
	Run 2	-0.364	-0.0024	-0.0136
	Run 3	-0.398	-0.0036	-0.0110
	Average	$-363.1 *10^{-3}$ N	$-6.87 *10^{-3}$ Nm	$1.31 *10^{-3}$ Nm
	Range	0.142 N	0.0082 Nm	0.0258 Nm

Table C.1: Base Nose, Base Tail

		Drag	Downforce	Yaw
Test 1	Run 1	-0.354	-0.0202	0.0060
	Run 2	-0.376	-0.0180	-0.0036
	Run 3	-0.334	-0.0180	-0.0034
Test 2	Run 1	-0.310	-0.0188	-0.0040
	Run 2	-0.354	-0.0186	0.0080
	Run 3	-0.378	-0.0196	0.0004
Test 3	Run 1	-0.372	-0.0180	0.0010
	Run 2	-0.406	-0.0118	-0.0140
	Run 3	-0.366	-0.0174	0.0010
	Average	-361.1 $*10^{-3}$ N	-17.82 $*10^{-3}$ Nm	-0.96 $*10^{-3}$ Nm
	Range	0.096 N	0.0084 Nm	0.022Nm

Table C.2: High Nose, Base Tail

		Drag	Downforce	Yaw
Test 1	Run 1	-0.374	-0.0128	0.0078
	Run 2	-0.386	0.0002	-0.0106
	Run 3		Run aborted	
Test 2	Run 1	-0.390	-0.0100	0.0178
	Run 2	-0.362	-0.0088	0.0116
	Run 3	-0.438	-0.0100	0.0130
Test 3	Run 1	-0.390	-0.0084	0.0118
	Run 2	-0.332	-0.0074	0.0034
	Run 3	-0.444	-0.0094	0.0050
	Average	-389.5 $*10^{-3}$ N	-8.32 $*10^{-3}$ Nm	7.47 $*10^{-3}$ Nm
	Range	0.112 N	0.0054 Nm	0.0284 Nm

Table C.3: Long Nose, Base Tail

C.1.2 Tail configurations

		Drag	Downforce	Yaw
Test 1	Run 1	-0.386	-0.0126	0.0082
	Run 2		Run aborted	
	Run 3	-0.362	-0.0140	0.0134
	Run 4	-0.290	-0.0140	0.0108
	Run 5	-0.392	-0.0130	0.0042
	Run 6	-0.410	-0.0152	0.0116
Test 2	Run 1	-0.395	-0.0114	0.0114
	Run 2	-0.458	-0.0142	0.0106
	Run 3	-0.374	-0.0128	0.0088
	Run 4	-0.328	-0.0128	0.0066
	Run 5	-0.400	-0.0112	0.0104
	Run 6	-0.292	-0.0142	0.0104
	Run 7	-0.376	-0.0134	0.0088
	Average	$-371.9 *10^{-3}$ N	$-13.2 *10^{-3}$ Nm	$9.6 *10^{-3}$ Nm
	Range	0.168 N	0.0040 Nm	0.0092 Nm

Table C.4: Base Tail, Base Nose

		Drag	Downforce	Yaw
Test 1	Run 1	-0.424	-0.0166	0.0174
	Run 2	-0.372	-0.0102	0.0164
	Run 3		Run aborted	
	Run 4	-0.330	-0.0152	0.0164
	Run 5	-0.354	-0.0162	0.0122
	Run 6	-0.380	-0.0152	0.0116
Test 2	Run 1	-0.256	-0.0162	0.0216
	Run 2	-0.352	-0.0162	0.0180
	Run 3	-0.372	-0.0184	0.0174
	Run 4	-0.420	-0.0156	0.0154
	Run 5	-0.382	-0.0160	0.0148
	Run 6	-0.338	-0.0152	0.0146
	Run 7	-0.308	-0.0150	0.0184
	Average	$-357.3 *10^{-3}$ N	$15.5 *10^{-3}$ Nm	$16.2 *10^{-3}$ Nm
	Range	0.168 N	0.0082 Nm	0.0100 Nm

Table C.5: +60mm Tail, Base Nose

C.2   Increasing AoA data

Due to the size of the data compiled, this table is just the max, min and average obtained. Complete data is available if needed.

Angle		Fx (N)	Fy (N)	Tx (Nm)	Ty (Nm)	Tz (Nm)
0.5	Max	0.410	0.140	0.006	0.013	0.110
0.5	Ave	0.316	0.015	0.003	0.005	0.018
0.5	Min	0.210	-0.130	0.000	-0.002	0.001
1.5	Max	0.420	0.310	0.012	0.015	0.050
1.5	Ave	0.356	0.223	0.008	0.011	0.041
1.5	Min	0.220	0.110	0.004	0.008	0.027
3.0	Max	0.270	0.610	0.019	0.007	0.102
3.0	Ave	0.147	0.511	0.015	0.004	0.091
3.0	Min	0.040	0.420	0.010	0.000	0.081
5.0	Max	0.280	0.900	0.020	-0.005	0.130
5.0	Ave	0.258	0.864	0.019	-0.006	0.126
5.0	Min	0.220	0.840	0.017	-0.007	0.122

Table C.6: Base tail, base nose

Angle		Fx (N)	Fy (N)	Tx (Nm)	Ty (Nm)	Tz (Nm)
0.5	Max	0.370	0.130	0.006	0.015	0.038
0.5	Ave	0.277	-0.019	0.004	0.012	0.024
0.5	Min	0.220	-0.180	0.002	0.008	0.015
1.5	Max	0.460	0.370	0.009	0.018	0.059
1.5	Ave	0.361	0.189	0.006	0.010	0.044
1.5	Min	0.280	0.020	0.002	0.004	0.029
3.0	Max	0.420	0.610	0.019	0.010	0.109
3.0	Ave	0.294	0.471	0.014	0.007	0.101
3.0	Min	0.220	0.380	0.012	0.004	0.092
5.0	Max	0.340	1.060	0.024	-0.008	0.159
5.0	Ave	0.270	1.012	0.021	-0.027	0.156
5.0	Min	0.210	0.970	0.018	-0.099	0.153

Table C.7: Base tail, long nose

Angle		Fx (N)	Fy (N)	Tx (Nm)	Ty (Nm)	Tz (Nm)
0.5	Max	0.400	-0.030	0.004	0.019	0.038
0.5	Ave	0.335	-0.093	0.003	0.014	0.028
0.5	Min	0.240	-0.240	0.001	0.007	0.021
1.5	Max	0.470	0.290	0.011	0.017	0.056
1.5	Ave	0.358	0.195	0.008	0.013	0.022
1.5	Min	0.230	0.120	0.005	0.008	-0.056
3.0	Max	0.450	0.630	0.013	0.015	0.084
3.0	Ave	0.349	0.572	0.012	0.007	0.079
3.0	Min	0.250	0.490	0.010	0.005	0.073
5.0	Max	0.340	1.150	0.021	-0.009	0.122
5.0	Ave	0.282	1.078	0.020	-0.012	0.118
5.0	Min	0.240	1.030	0.019	-0.014	0.115

Table C.8: High tail, long nose

Angle		Fx (N)	Fy (N)	Tx (Nm)	Ty (Nm)	Tz (Nm)
0.5	Max	0.450	-0.010	0.007	0.019	0.035
0.5	Ave	0.336	-0.120	0.004	0.012	0.022
0.5	Min	0.230	-0.340	0.000	0.006	0.008
1.5	Max	0.420	0.270	0.015	0.017	0.044
1.5	Ave	0.308	0.128	0.009	0.015	0.040
1.5	Min	0.200	0.020	0.005	0.011	0.035
3.0	Max	0.420	0.570	0.016	0.012	0.077
3.0	Ave	0.317	0.480	0.012	0.009	0.071
3.0	Min	0.190	0.340	0.010	0.006	0.066
5.0	Max	0.390	1.010	0.019	-0.010	0.101
5.0	Ave	0.358	0.992	0.018	-0.011	0.096
5.0	Min	0.330	0.980	0.017	-0.012	0.091

Table C.9: High tail, base nose

Appendix D

Technical information

D.1 Nano 25 F/T transducer

◉ 16-Bit DAQ and Net F/T System ○ Controller F/T System

Standard Calibrations (US)

Calibration	Fx,Fy	Fz	Tx,Ty	Tz	Fx,Fy	Fz	Tx,Ty	Tz
US-25-25	25 lbf	100 lbf	25 lbf-in	25 lbf-in	1/224 lbf	3/224 lbf	1/160 lbf-in	1/320 lbf-in
US-50-50	50 lbf	200 lbf	50 lbf-in	30 lbf-in	1/112 lbf	3/112 lbf	1/80 lbf-in	1/160 lbf-in
	SENSING RANGES				RESOLUTION			

View Standard (US) Complex Loading Graph

Metric Calibrations (SI)

Calibration	Fx,Fy	Fz	Tx,Ty	Tz	Fx,Fy	Fz	Tx,Ty	Tz
SI-125-3	125 N	500 N	3 Nm	3 Nm	1/48 N	1/16 N	1/1320 Nm	1/2640 Nm
SI-250-6	250 N	1000 N	6 Nm	3.4 Nm	1/24 N	1/8 N	1/660 Nm	1/1320 Nm
	SENSING RANGES				RESOLUTION			

Figure D.1: Ranges for the ATI Nano25 F/T transducer [12]

The transducer used for these experiments is the SI-250-6.

Single-Axis Overload	
Fxy	±2300 N
Fz	±7300 N
Txy	±43 Nm
Tz	±63 Nm
Stiffness (Calculated)	
X-axis & Y-axis forces (Kx, Ky)	5.3×10^7 N/m
Z-axis force (Kz)	1.1×10^8 N/m
X-axis & Y-axis torque (Ktx, Kty)	6.5×10^3 Nm/rad
Z-axis torque (Ktz)	9.2×10^3 Nm/rad
Resonant Frequency	
Fx, Fy, Tz	3600 Hz
Fz, Tx, Ty	3800 Hz
Physical Specifications	
Weight*	0.0634 kg
Diameter*	25 mm
Height*	21.6 mm

* Specifications include standard interface plates.

Figure D.2: Specifications for the ATI Nano25 F/T transducer [12]

D.2   Tooling board details

Tooling, Modelling and Styling boards: Selection Guide

Stock Items

For data sheets click on product name

Product	Application	Diamentions	Colour	Density (g/cm³)	Shore Hardness (ISO 868)	Compressive strength (ISO 604) (MPa)	Compressive modulus (ISO 604) (MPa)	Coefficient of thermal Expansion (DIN 53752) (10-6 K-1)	Deflection temperature (ISO 75) (°C)
RenShape® BM 5108	Design studies, program proving, supporting structures	2500x1200x100 2500x1200x200	White	0.08					
RenShape® BM 5120	Styling models, Styling, Milling program proving	1500 x 400 x 100	Light grey	0.25		4 - 5		50-60	60
RenShape® BM 5185	Styling and master models	1500x500x50 1500x500x100	Apricot or Brown	0.47		10-15	500-600	60-65	60-70
RenShape® BM 5440	Master models, cubing models, patterns etc.	1500x500x50 1500x500x100	Brown	0.5	55-60 D	15-20	600-700	50-55	75-80
RenShape® BM 5460	Master models, cubing models, patterns etc.	1500x500x25 1500x500x50 1500x500x100 1500x500x200	Brown	0.7	60-65 D	20-25	910-960	50-55	75-80
RenShape® BM 5172	Pattern plates and core boxes, negative moulds and tools	1000x500x50 1000x500x100	Green	1.2	80 D	60-70	1900-2000	80-85	80-90
RenShape® BM 5272	Pattern plates and core boxes, machined negatives / positives, models, moulds and tools	1000x500x50 1000x500x75 1000x500x100	Olive	1.4	80-85 D	70-80	3300-3500	65-70	80-90

Figure D.3: Details of the Renshape tooling board from Meury
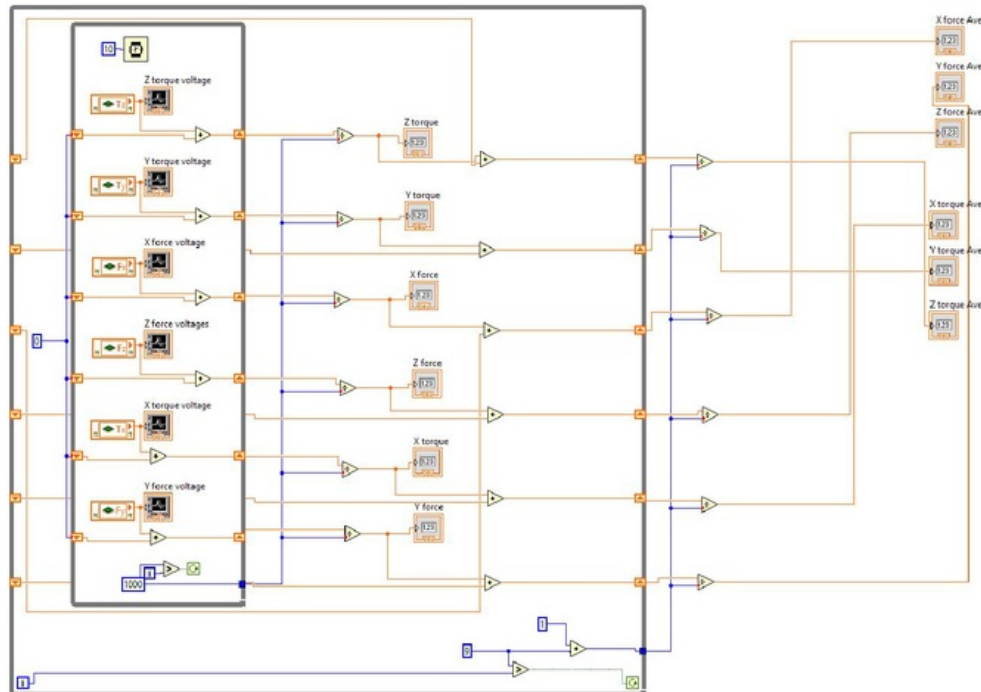
D.3   Labview coding

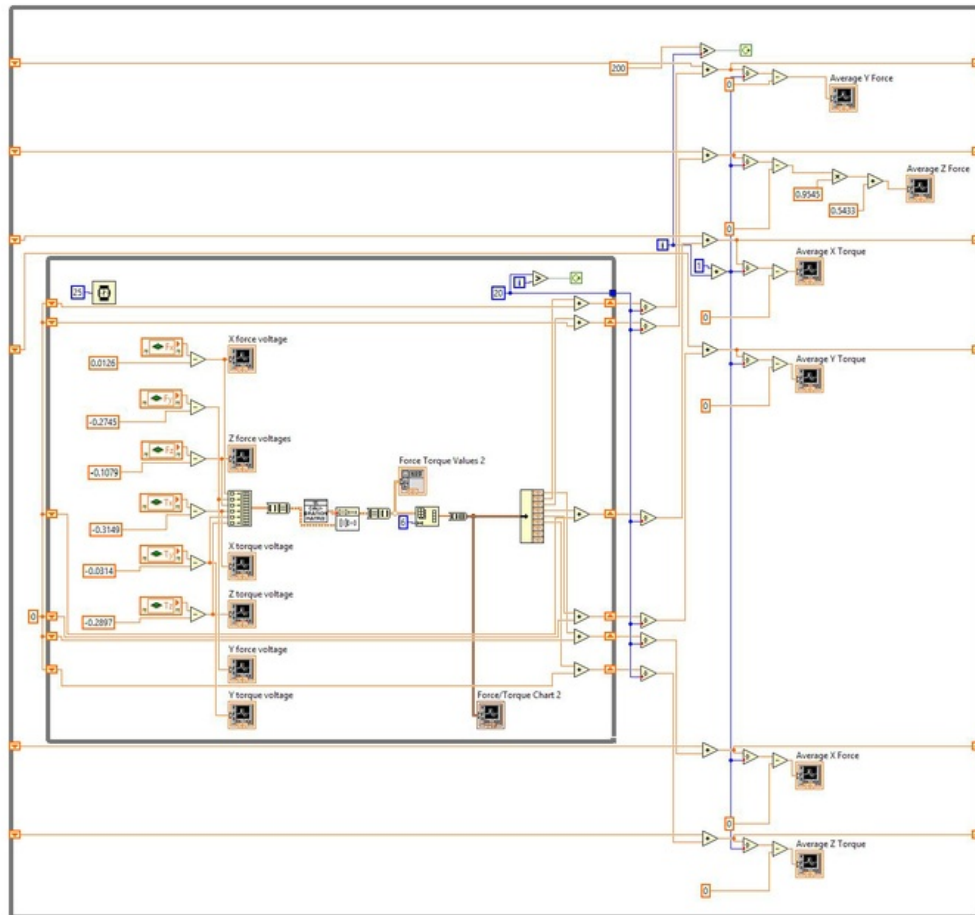**Figure D.4:** LabVIEW routine for calabration and baseline values for the Nano25

Figure D.5: LabVIEW coding for monitoring the F/T transducer output

Appendix E

Information for continuing experimentation

E.1 Tasks to be completed before continuing

During the initial testing for this project some issues appeared that were not able to be resolved in the time available. If these can be resolved the continuing project will generate better data.

- *Consolidate the MyRIO instrumentation into the cRIO board.*
  Previous projects had established control features and software for the wind tunnel via the MyRIO board. Another project had validated that the F/T transducer operated and obtained data via the cRIO system. When these two systems were run at the same time they interfered with each other meaning that manual adjustments to the wind speed had to be made to enable F/T data to be obtained.

- *Track down the EMI interference from the wind tunnel.*
  When the F/T transducer was placed within the tunnel for the first time is showed massive EMI (ElectroMagnetic Interference) which rendered the transducer inoperable. This interference was reduced by removing the network cabling from the control computer and isolating the stop button wiring from the data cabling.

E.2 Operating the LabVIEW software

- *QuickCal.*
  The LabVIEW QuickCal program was my method for zeroing the initial forces acting on the F/T transducer. It works by averaging the six voltage outputs collected by the transducer and feeding these back into the data collection program as a subtraction offset. Just run the program until it stops and collect the offsets given at the end.

- *F/T averaging program.*
  This program was devised to compensate for the noisy signal being obtained from

77

the F/T transducer. When it is initially opened, the block diagram section should be opened and the offset figures obtained by QuickCal are directly input into the input boxes and then save the program.

Set the windspeed desired and run the averaging program. The program was run five times for each data set to allow further averaging. This can be altered depending on new information.

- *Re-validate the averaging program.*
  As the program was established to compensate for the EMI noise, any change in the circumstances associated with the EMI should mean re-validation of the program is needed.

E.3   The model

- *Changing parts.*
  The center hood should be lifted when changing nose and tail sections as this section is slightly wedge shaped and is designed to lock in the ends as it is wound down.

- *Model issues.*
  It was intended to insert helicoils into the mounting areas of the model but this wasn't achieved. Replacing the current screws with helicoil inserts and bolts will increase the longevity of the model for future experimentation.

Appendix F

Consultation meetings

Consultation Meetings Attendance Form
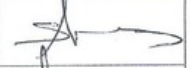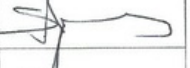
Week	Date	Comments (if applicable)	Student's Signature	Supervisor's Signature
1	1/8/16	DISCUSSED FINALISED INTERNAL STRUCTURE	Geoff RA	
2	10/8/16	NSW SCIENCE FAIR AND MILLING MODEL	Geoff RA	
3	17/8/16	WIND TUNNEL AND SENSORS	Geoff RA	
4	25/8/16	CALABRATION AND THESIS CHAPTERS	Geoff RA	
5	1/9/16	INSTALATION OF MODEL IN WIND TUNNEL	Geoff RA	
6	8/9/16	PROGRESS REPORT + MODEL PIECES	Geoff RA	
7	15/9/16	SOLVING EM INTERFERENCE ISSUES	Geoff RA	
BREAK	22/9/16	FIRST SET OF TEST DATA FROM BASE MODEL	Geoff RA	
8	6/10/16	RELATE HOW DATA TO BE USED, IDEAS	Geoff RA	
10	19/10/16	DISCUSS YAW DATA " PIV	Geoff RA	
11	26/10/16	DISCUSS LAYOUT OF THESIS WORK	Geoff RA	
12	30/10/16	FINAL THESIS THOUGHTS	Geoff RA	

**Figure F.1:** Attendance form for consultation meetings

Appendix G

Alternative Timeline Gantt Chart

Tasks associated with the Gantt chart timeline

1. Sensor Selection

2. Sensor Procurement

3. Sensor Calibration

4. Shell Design

5. Construction

6. Test session 1

7. Test session 2

8. Test session 3

9. Test session 4

10. Consolidate data

11. Supply data for CFD

12. Write up thesis

13. Assessment tasks
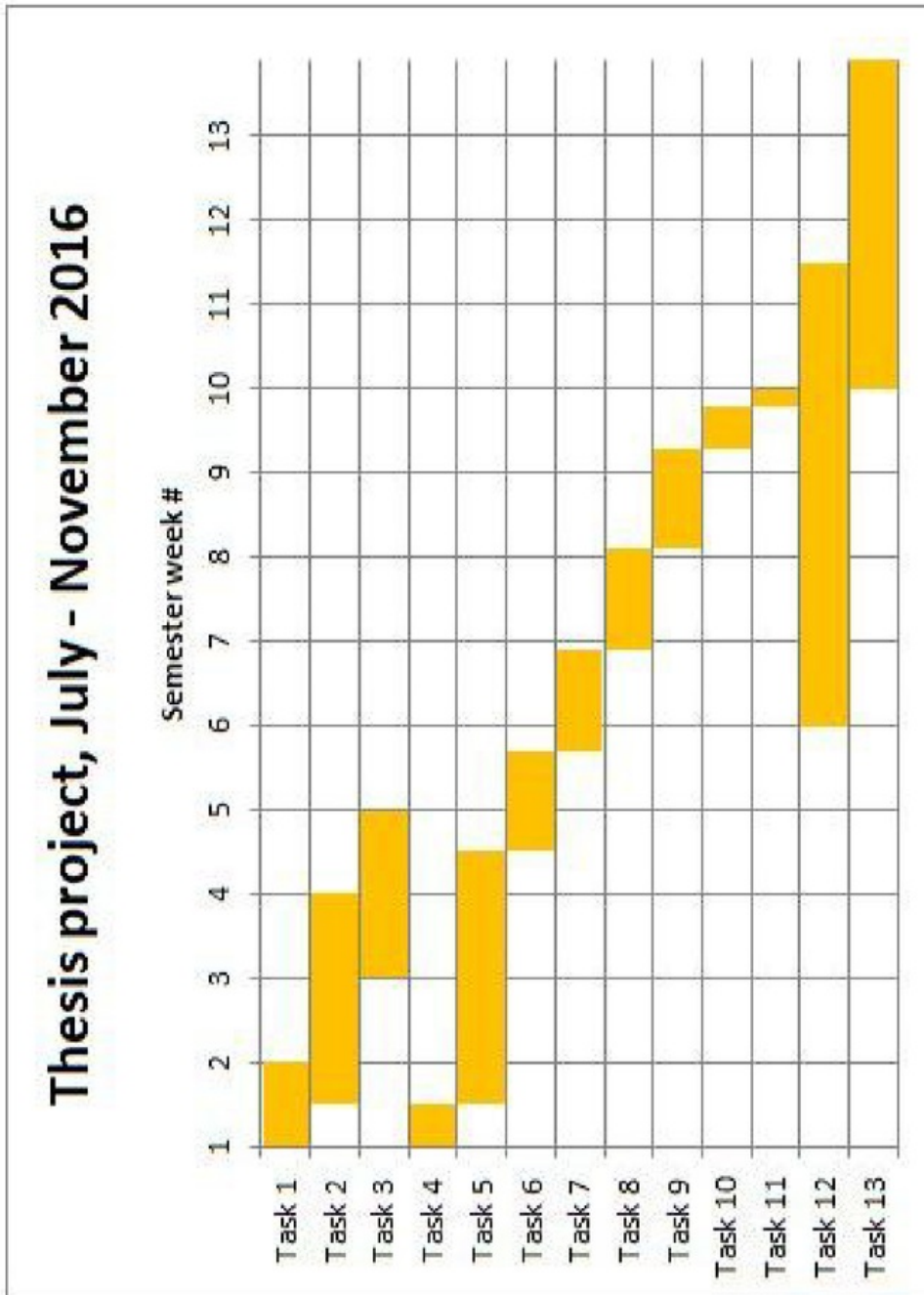
Appendix H

Recent world record breaking teams

Record (km/h)	Team	Designer	Rider	Year
144.17	Eta	Aerovelo	Todd Reichert	09/17/16
139.45	Eta	Aerovelo	Todd Reichert	09/19/15
133.78	Velox 3	Delft	Sebastiaan Bowier	09/14/13
133.28	Varna Tempest	Georgi Georgiev	Sam Whittingham	09/18/09
132.50	Varna Diablo 3	Georgi Georgiev	Sam Whittingham	09/18/08
130.36	Varna Diablo II	Georgi Georgiev	Sam Whittingham	10/5/02
129.64	Varna Diablo	Georgi Georgiev	Sam Whittingham	10/6/01

Table H.1: Recent world record breaking speeds [11].

Bibliography

[1] T. Aerovelo. (2016, Sept.) Team aerovelo. [Online]. Available: http://www.aerovelo. com/

[2] F. Alam, S. Pedro, and G. Zimmer, "Aerodynamic study of human powered vehicles," *Procedia Engineering*, vol. 34, pp. 9–14, 2012.

[3] F. Alam, H. Chowdhury, E. Guillaume, J. Yang, and G. Zimmer, "On-road and wind tunnel aerodynamic study of human powered vehicles," *Procedia Engineering*, vol. 60, pp. 473 – 478, 2013.

[4] H. Chowdhury and F. Alam, "Bicycle aerodynamics: an experimental evaluation methodology," *Sports Engineering*, vol. 15, no. 2, pp. 73–80, 2012. [Online]. Available: http://dx.doi.org/10.1007/s12283-012-0090-y

[5] H. Chowdhury, F. Alam, S. Arena, and I. Mustary, "An experimental study of airflow behaviour around a standard 2-man bobsleigh," *Procedia Engineering*, vol. 60, pp. 479 – 484, 2013.

[6] T. Defraeye, B. Blocken, E. Koninckx, P. Hespel, and J. Carmeliet, "Aerodynamic study of different cyclist positions: Cfd analysis and full-scale wind-tunnel tests," *Journal of Biomechanics*, vol. 43, no. 7, pp. 1262–1268, 2010. [Online]. Available: http://dx.doi.org/10.1016/j.jbiomech.2010.01.025

[7] T. Delft. (2016, October) Testing velox 6. [Online]. Available: http://basdemeijer.photoshelter.com/portfolio/C0000oBYbUT4CLB0/ G0000R6.7fHkjwmE/I0000YwPZk99O1no

[8] EngineeringToolbox. (2016, Nov) Pitot tubes. Engineering Toolbox. [Online]. Available: http://www.engineeringtoolbox.com/pitot-tubes-d_612.html

[9] H. K. Epema, S. v. d. Brand, W. Gregoor, J. D. G. Kooijman, H. P. Pereboom, D. C. Wielemaker, and C. J. v. d. Zweep, "Bicycle design: A different approach to improving on the world human powered speed records," *Procedia Engineering*, vol. 34, pp. 313 – 318, 2012.

[10] A. R. Flight. (2016, Sept.) Airplane turning tendencies. [Online]. Available: http://allrcflight.com/airplane-turning-tendencies/

[11] IHPVA. (2016, October) Ihpva, men's 200 meter flying start speed trial - single rider. IHPVA. [Online]. Available: http://www.ihpva.org/hpvarecl.htm#nom01

[12] A. industrial automation. (2016, Aug) F/t sensor: Nano25. Website. ATI industrial automation. [Online]. Available: http://www.ati-ia.com/products/ft/ft_models.aspx?id=Nano25

[13] C. R. Kyle and M. D. Weaver, "Aerodynamics of human-powered vehicles," *Proceedings of the Institution of Mechanical Engineers, Part A: Journal of Power and Energy*, vol. 218, no. 3, pp. 141–154, 2004. [Online]. Available: http://pia.sagepub.com/content/218/3/141.abstract

[14] Meury. (2016, Aug) Rapid prototyping boards. Meury Pty. Ltd. [Online]. Available: http://meury.com.au/our-products/tooling-boards/

[15] M. M. Munk, "General theory of thin wing sections," National Advisory Committee for Aeronautics; Washington, DC, United States, Tech. Rep., Jan 01, 1923.

[16] NI. (2016, Sept.) The compactrio platform. National Instruments. [Online]. Available: http://www.ni.com/compactrio/

[17] Rathbones. (2016, September) Arion2 breaks british land speed records. University of Liverpool Velocipede Team. [Online]. Available: https://www.rathbones.com/knowledge-and-insight/arion2-breaks-british-land-speed-records

[18] D. M. Roche and UNSW., *Speed of light : the 1996 World Solar Challenge / D. M. Roche ... [et al.].* Photovoltaics Special Research Centre Sydney, 1997, vol. Chapter 5, Pg. 92.

[19] S. Wangerin, S. Lillywhite, and C. Davis, "Aerodynamic test platform for human powered vehicle (hpv)," Thesis, California Polytechnic State University at San Luis Obispo, 2012.